ABSTRACT

FUNDERBURK, MORGAN LEE. Experimental Investigation of Primary and Corner Shock Boundary Layer Interactions at Mild and Increasing Back Pressure Ratios. (Under the direction of Dr. Venkateswaran Narayanaswamy).

An experimental investigation is undertaken with the objective of elucidating the shock boundary layer interactions (SBLI) in rectangular inlets that occur prior to unstart initiation. Measurements are taken along the interactions between incoming floor and corner boundary layers with an oblique shock wave generated by a compression ramp in a rectangular channel at Mach 2.5. The oblique shock strength is amplified by increasing the flow turn angle between tests, which simulates the pressure rise caused by combustion-induced heat release during unstart. The resulting back pressure ratio falls between $30 - 55\%$ of the normal shock ratio. Qualitative surface streakline visualization is used to resolve the mean features of the shock-induced separation structures and deduce the fluid kinematics of the floor (primary) and corner SBLI units. High-resolution, high-frequency wall pressure measurements are also taken to gain a quantitative understanding of the mean and unsteady pressure fields. Subsequently, statistical cross-coherence techniques are utilized to determine the degree of coupling between wall pressure fluctuations at various positions in the flowfield to determine the evolution of the driving mechanisms of the primary and corner SBLI with increasing back pressure. Results suggest a transition from locally driven, uncoupled units to a global unstart shock system with increasing back pressure ratio.

Experimental Investigation of Primary and Corner Shock Boundary Layer Interactions at Mild and Increasing Back Pressure Ratios

by
Morgan Lee Funderburk

A thesis submitted to the Graduate Faculty of
North Carolina State University
in partial fulfillment of the
requirements for the degree of
Master of Science

Aerospace Engineering

Raleigh, North Carolina

2016

APPROVED BY:

_____	_____
Dr. Jack Edwards	Dr. Pramod Subbareddy

_____
Dr. Venkateswaran Narayanaswamy
Chair of Advisory Committee

ACKNOWLEDGMENTS

I would like to thank my graduate advisor, Dr. Venkateswaran Narayanaswamy, who has provided me with a wealth of knowledge and guidance in the areas of inlet unstart and shock boundary layer interaction, and has helped to develop my professional skillset as an engineer and researcher in the field of fluid dynamics. I similarly extend my gratitude to all members of the graduate faculty who provided me with direction and assistance at times while pursuing my degree, to include the specialty trades technicians and service coordinators, without whom none of the present work would have been possible. To my parents, who have loved and enabled me throughout my life, who have instilled in me a strong work ethic, and who have taught me to realize the value of an education, I am forever grateful. To all of my family members and the numerous friends who have been emotional pillars for me over the course of my education, I am indebted and thoroughly thankful for your support.

TABLE OF CONTENTS

LIST OF TABLES

LIST OF FIGURES

I. INTRODUCTION

A. Historical context and background

Ramjet and scramjet type engines represent the future of air-breathing propulsion, enabling flight at extreme altitudes and hypersonic velocities with greatly improved specific impulses when compared to the conventional rocket engine [1]. This improvement is a result of bypassing the weight penalties associated with the payload of oxidizer necessary onboard a rocket powered vehicle. Ram/scramjets instead achieve the necessary mass flow rate of oxidizer to the combustion chamber in a manner similar to that of conventional turbojet engines, namely the intake and compression of the low-density freestream air. The specific impulse of any type of air-breathing jet engine differs from that of a rocket engine in that it decreases with the flight Mach number, which acts to continually increase the stagnation temperature of the intake air and reduce combustion efficiency. Eventually, the use of a conventional compressor section (like those seen in turbojet engines), becomes impractical at higher flight Mach numbers as it acts to further increase the stagnation temperature of air entering the combustion chamber through the addition of work energy.

In order to curb this effect, ram/scramjet engines instead sustain compression by passing the intake air through adiabatic oblique shock wave trains. This enables them to outperform turbojet engines for flight Mach numbers in excess of 3. A ramjet will generally outperform a scramjet until approximately Mach 6, when the terminating normal shock in a ramjet isolator begins to introduce losses more significant than those associated with the inefficiencies of supersonic combustion [1]. Consequently, the scramjet provides superior efficiencies to flight Mach numbers that are as of yet unknown (although it is suspected that

the ever-increasing stagnation temperature of the intake air will eventually reduce scramjet efficiency to rocket-like levels). Subsequently, there is a desire to use ram/scramjet type engines onboard vehicles capable of low-earth-orbits (LEOs) for exponentially decreased transportation times and the potential insertion of payloads into orbit. There are however, several important implications associated with the use of such engines. One such implication is the inability of the ram/scramjet engine to produce static thrust, as they require the incoming air to be supersonic to generate compression. Therefore, a vehicle that is powered by a ram/scramjet will need to utilize a multi-mode engine to produce thrust from takeoff, employing a conventional turbojet at subsonic and low supersonic flight Mach numbers, before transitioning to ramjet and finally scramjet operation with increasing airspeed. These hypothetical vehicles have become known as the air-breathing single-stage-to-orbit (SSTO) concept.

In reality, when considering the complexity of the proposed multi-mode engines onboard an SSTO, it becomes evident that the elimination of the intermediate ramjet phase is desirable. This elimination both cuts down on the total complexity of the propulsion system (eliminating potential points of failure) and reduces weight, providing two key engineering benefits. Therefore, the scramjet phase must start at reduced flight Mach numbers. Again, there is a serious implication associated with such a reduction in starting speed. For scramjet operations at flight Mach numbers less than 7, the inlet compression coupled with the downstream temperature rise due to combustion-induced heat release can create a back pressure significant enough to eject the stabilized oblique shock train from the inlet altogether in a sweeping motion known as an unstart [2]. The discharge of the oblique shock train from

the inlet immediately results in a massive loss of thrust and a large transient mechanical loading that can couple with the resonant frequencies of airframe structures, causing severe damage and potential loss of the aircraft.

While many other difficult technologies must be solved in order to make sustained hypersonic SSTO flights a reality, the unstart problem is not merely confined to future scenarios. In reality, the issue is over five decades old. Some of the earliest reports of unstart came during the initial flights of the SR-71 Blackbird, a supersonic surveillance platform that utilized two J58 "turbo-ramjets," which at cruise Mach numbers of 3.2 would bypass a compressor stage and inject air directly into the combustion chamber via a series of ducts. In 1966, an SR-71 experienced significant asymmetric thrust issues due to a right-side unstart event while cruising at over 80,000 feet, resulting in the breakup and loss of the aircraft [3]. This event prompted the inlet designers of the SR-71 to address the unstart issue, although the eventual solution did not directly prevent the occurrence of unstart [4]. It instead consisted of

Figure 1. An SR-71 attempts a right-side restart after engine failure.

a sympathetic unstart generator that could reduce power to the unaffected engine so that asymmetric thrust could not cause loss of vehicle control before the engine could be re-started.

Similarly, unstart events have impeded the recent flight-testing of highly experimental scramjet testbed vehicles like the Boeing X-51 Waverider [5]. The difficulty and persistence of the unstart issue in the past and present necessitate a thorough investigation into both the unstart process itself and the driving mechanisms of unstart in order to gain an understanding that will aid in the development of eventual control and prevention methodologies. These methodologies will expand the operating margins of the next generation of hypersonic air-breathing vehicles.

B. Past investigations into unstart dynamics

1. Unstart process

A number of efforts have attempted to characterize the unstart process. Early experimental studies generally consisted of rectangular inlet sections with unstart induced by mechanical throttling of the flow that simulated the combustion-induced back pressure rise discussed in [2]. Wieting [6], who induced unstart through the insertion of a cylindrical pin in a downstream portion of the isolator, reported the formation of a normal unstart shock system just upstream of the pin which was seen to propagate upstream at $1-4\%$ of the freestream velocity, u_∞ (in the laboratory reference frame). The maximum mechanical loading along the inlet walls occurred with the passage of the unstart shock system, which eventually stabilized at a position upstream of the cowl lip allowing for mass spillage around the inlet. Interestingly, the terminal unstart shock observed was oblique in nature rather than normal near the inlet

wall. This difference was attributed to the shock boundary layer interaction (SBLI) along the sidewall which, through boundary layer separation due to the shock-induced adverse pressure gradient, acted to bifurcate the near-wall normal shock into a λ-structure consisting of an oblique compression wave and a reflected wave. This compression wave propagated upstream with the boundary layer separation until the normal shock structure was no longer evident.

Wagner et al. [7] corroborated the establishment and upstream propagation phases of the unstart shock system observed by Wieting [6] in an unstart event triggered by raising a flap in the downstream portion of a dual-mode scramjet isolator. An oblique shock formed upstream of the flap, and resulted in an SBLI-induced separation shock along the opposite wall. This pair of opposing oblique shock waves formed the unstart shock system, which was seen to propagate upstream through the isolator for a time while coalescing with the stabilized shock train, before slowing to match the speed at which the ceiling boundary layer separation propagated, as shown in Figure 2. The near-wall unstart shock structure was seen to increasingly bifurcate during this propagation, indicating an increase in boundary layer separation. The unstart shock system then accelerated to $0.10\,u_\infty$ upon reaching the converging portion of the inlet before entering into an oscillatory motion in and out of it, which was attributed to an acoustic resonator phenomenon associated with a system of reflecting compression waves in the isolator, the bulk flow of which was highly separated. The cycle of

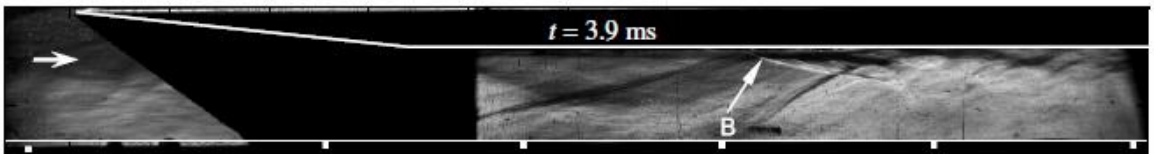

Figure 2. Propagation of unstart shock system (denoted by arrow B). Figure adapted from Wagner et al. [7].

motion of the isolator waves was correlated with an oscillatory mechanical loading, the amplitude of which was a function of the effective area contraction induced by the downstream flap.

It is interesting to observe how the unstart processes induced by mechanical throttling [6, 7] compare to those prompted by actual downstream combustion. O'Byrne et al. [8], who observed unstart in a strut-injection hydrogen fueled scramjet across a range of equivalence ratios, reported a process highly similar to those seen in the aforementioned works. A normal unstart shock system was initially seen to form at the intersection of the reflected injection wake shocks, which then increased in strength before propagating upstream. Increased boundary layer separation along the inlet floor and ceiling was observed during the transient portion of the unstart process, although the increasing wall bifurcation reported in [6] and [7] was not detected. Subsequently, O'Byrne et al. [8] concluded that while the unstart process itself was nominally the same, it was likely induced by a different driving mechanism, namely thermal choking due to heat release (to be discussed in the following section).

A second exploratory investigation of combustion-induced unstart in a scramjet engine was performed by Laurence et al. [9]. The process observed was highly consistent with all of the previously discussed studies. Again, an unstart shock system was seen to form in a downstream portion of the isolator/combustor duct before an upstream propagation occurred. Interestingly, simultaneous Schlieren and OH chemiluminescence showed a bulging combustion region that extended upstream of the propagating unstart shock, hugging the opposite wall shown here in Figure 3. It was postulated that this may be due to increased boundary layer separation along the duct floor, which would tend to cause increased turbulent

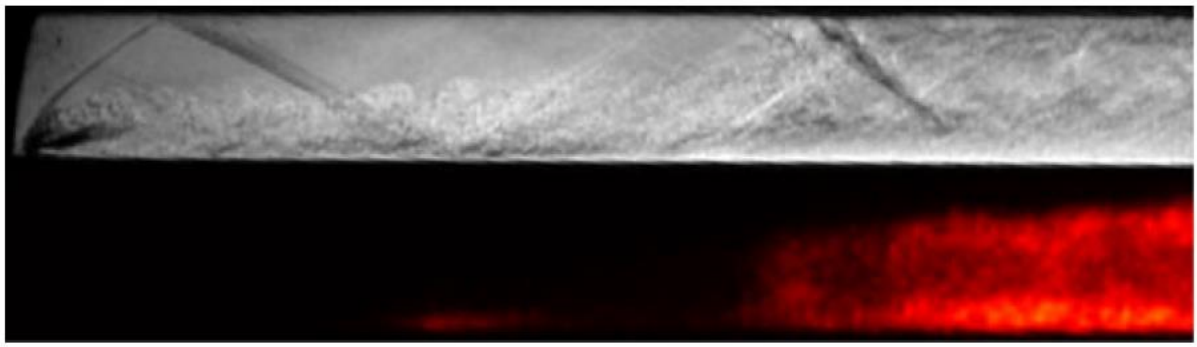

Figure 3. Simultaneous Schlieren (top) and OH chemiluminescence (bottom) during unstart propagation. Figure adapted from Laurence et al. [9].

mixing and sustain ignition. However, the unstart shock system observed also showed minimal distortion near the wall (similar to the findings reported by O'Byrne et al. [8]). The unstart shock also exhibited a momentary quasi-steady state during propagation, pausing momentarily at a location midway through the isolator before exiting the inlet.

The preceding discussion shows that, irrespective of the initiating mechanism (be it mechanical throttling or actual combustion), the reported unstart process is highly consistent across a range of studies. During the initiation phase an unstart shock system forms at a downstream portion of the isolator, although the structure of this shock system can vary considerably depending on the initiating mechanism. This shock system then propagates upstream, generating large mechanical loads at the inlet walls that are generally oscillatory in nature. This propagation is accompanied by increasing boundary layer separation near the walls, which may act to distort the moving shock. Once the unstart shock reaches a steady state in or upstream of the inlet mouth, the flow in the isolator/combustor is no longer supersonic and highly separated. Thus, there is an obvious need to further investigate the causes behind the formation and upstream sweep of the unstart shock system for mitigation purposes.

2. Driving mechanisms of unstart process

In the previously discussed experimental studies that describe the initiation and perpetuation phases of the unstart process [6, 7, 8, 9], an interesting dichotomy arises with respect to the causal mechanisms reported. In the case of Wieting [6], shock-induced boundary layer separation was seen to drive the upstream propagation of the unstart shock system and determine its terminal shape. Furthermore, the unstart shock system of Wagner et al. [7] consisted of a boundary layer separation shock along the ceiling of the isolator. Therefore, it would seem that shock boundary layer interactions (SBLI) play a prominent role in both the formation and propagation of the unstart shock system when the process is caused by aerodynamic choking. However, in the studies where unstart was induced via combustion of hydrogen gas [8, 9], while the near wall shock structure was distorted during propagation, the classic λ-bifurcation was not evident. This lead to the supposition that thermal choking due to heat release was the culprit behind the formation of the unstart shock system.

In reality, the lack of a λ-structure is not enough to disqualify mechanical throttling as a potential cause of unstart shock formation in the combustion studies. The Schlieren images utilized are line-of-sight integrated along the span of the inlet/isolator, making it difficult to resolve the structure of the unstart shock system near the inlet corners and sidewalls. It is within the realm of possibility that the boundary layers along the inlet corners and sidewalls in these studies are separated, which could induce aerodynamic choking and the subsequent formation phase. It is interesting to note that Frost et al. [10] performed a series of experiments in the same scramjet utilized by Laurence et al. [9] for nominally identical test conditions. The correlation developed by Korkegi [11] to determine the onset of incipient boundary layer

separation due to the shock-induced adverse pressure gradient proved to coincide very closely with the onset of choking for these tests across a range of flight Mach numbers. Further, a Rayleigh flow analysis was performed to determine the mass flow rate of hydrogen fuel needed to thermally choke the inlet, and it was found that the experimental mass flow rates were well below this value.

On the computational side, works by McDaniel & Edwards [12, 13] echo the schism in initiating mechanisms (between thermal and mechanical choking) observed in the experimental works. Initially, a domain based on a hydrogen fueled scramjet operated by the National Aerospace Laboratory (NAL) of Japan was tested across a range of equivalence ratios using two-dimensional (2D) numerics [12]. The results of the 2D simulations showed good agreement with experimental data compiled by NAL [14], and pointed to thermal choking as the cause of the unstart shock system formation. However, the later implementation of three-dimensional (3D) numerics revealed a large sidewall boundary layer separation induced by the fuel injection recompression shock [13]. This separation entrained hydrogen from the core flow and resulted in an upstream propagating reaction front (similar to the one described by Laurence et al. [9]), which the unstart shock system followed. This result indicates that the unstart event was entirely SBLI driven, occurring well before thermal choking could take place. It should be noted, however, that the turbulence model utilized in [13] may have a tendency to over-separate the sidewall boundary layers which could expedite this process.

Ultimately, neither thermal choking nor SBLI can be entirely discounted as mechanisms that commence unstart. However, it has been shown that in situations where no actual heat release is present, SBLI act as the sole initiator and produce an unstart process that

is highly consistent with those observed in actual combustion processes. Further, the relative lack of consensus as to whether SBLI are the instigating mechanisms behind the unstart of hydrogen-fueled scramjets seems to suggest that they cannot be ruled out in those scenarios. It is worth mentioning that these two choking processes refer solely to the devices behind the formation of the unstart shock system, comparatively little is known about the SBLI present in the propagation phase. In order to better understand the nature of the unstart-specific SBLI during the initiation and propagation phases, it will prove prudent to review the large body of research that has accumulated in this area.

C. Previous work in shock-boundary layer interactions

1. Two-dimensional shock boundary layer interactions

Due to the mounting importance of SBLI in both internal and external supersonic/ hypersonic flows, a great deal of work has accrued in this area over the last five decades, particularly in the area of 2D SBLI. In the interest of brevity, only a few of the results most relevant to unstart of rectangular inlets will be discussed here. For the interested reader, a number of reviews capture the progress made in 2D SBLI as a whole [15, 16, 17, 18, 19].

In general, 2D SBLI refer to the interactions between a shock wave and a canonical 2D compressible turbulent boundary layer. In the rectangular inlet/isolator of a scramjet, this definition applies loosely to the regions of the flow where the spanwise velocity is negligible. Due to the structure of the corner boundary layers that form at the junctions of the isolator floor/ceiling and sidewalls (to be discussed in the following section), only the boundary layers well away from the corner junctions can be considered 2D. Furthermore, the swept SBLI along

the sidewall share many characteristics with swept compression ramp and fin SBLI, and can be classified as 3D interactions [20]. Therefore, the use of the term 2D SBLI here is relegated to the impinging oblique shock train interactions along the isolator floor and ceiling.

In the impinging and reflected SBLI, the impinging wave angle dictates the strength of the adverse pressure gradient along the floor that the incoming boundary layer must traverse. If this adverse pressure gradient becomes too steep, a pocket of separated flow forms beneath the impinging shock (see Figure 4 for a schematic of the impinging SBLI flow features). This separation bubble is closed, in that the fluid within it recirculates [21]. Subsequently, the boundary layer upstream of the separation pocket lifts from the wall and turns to pass over the bubble, forming a separation shock wave which coalesces with the reflected shock. The separation shock wave penetrates the incoming boundary layer to the sonic line; this point of maximum penetration is known as the separation shock foot. Downstream of the separation bubble, the flow eventually reattaches to the wall and regains the characteristics of a 2D turbulent boundary layer, albeit with some alteration to its unsteady frequency content (to be

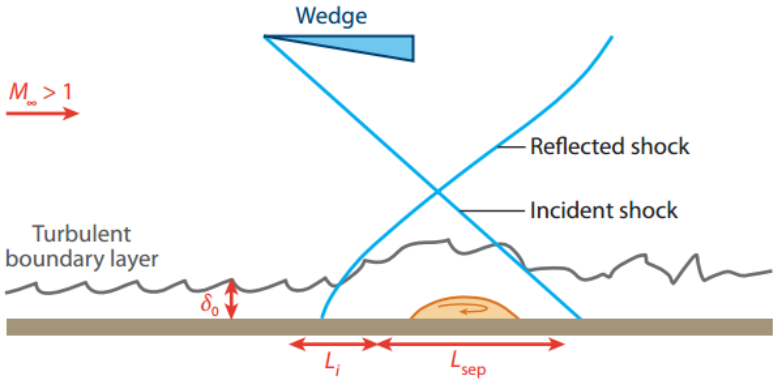

Figure 4. Impinging shock boundary layer interaction. Figure adapted from Clemens & Narayanaswamy [19].

discussed below). The length scale L_{sep} shown in Figure 4 is the distance between the point at which the boundary layer initially separates to cross the pocket of recirculating flow, and the point at which it reattaches downstream. It corresponds to the size of the separation bubble, and is influenced by the magnitude of the inviscid pressure gradient across the impinging/reflected shocks as well as the incoming turbulent Reynolds number, which is effectively a measure of the boundary layer's susceptibility to separation [19].

A salient feature of this type of SBLI is that it is highly unsteady, and induces fluctuating mechanical and thermal loads with frequencies considerably lower than those of the turbulent fluctuations in the incoming boundary layer, which are of the order u_∞/δ (where δ is the incoming boundary layer velocity thickness) [15]. Typically, u_∞/δ is in excess of several tens of kHz, whereas the characteristic unsteady motion of the SBLI is broadband and ranges from a few hundred Hz to several kHz. The oscillatory pressure loading is attributed to the unsteady motion of the separation shock foot, which traverses upstream and downstream across a maximum length scale L_i, depicted in Figure 4. Interestingly, across various interaction types with closed separation bubbles including impinging shock, compression ramp, and blunt fin SBLI, when the peak unsteady frequencies of the shock foot oscillation are nondimensionalized using L_i ($St_{Li} = \frac{f\,L_i}{u_\infty}$), they collapse into a range between $St_{Li} = 0.01 - 0.03$ [19]. This is significant, as it suggests that the physics behind the separation shock motions of closed SBLI are similar regardless of the downstream geometry. Therefore, a compression ramp SBLI is an effective analog for an impinging shock type interaction; this

greatly reduces the complexity of a conventional wind tunnel setup intended to study closed SBLI, which are akin to those seen during unstart.

Gramann & Dolling [22] performed wall pressure measurements beneath a 2D SBLI generated by a 28° compression ramp in a Mach 5 flow, and used two-point cross-correlation to show that the motions of the upstream separation shock were interconnected with motions of the downstream reattachment point. The separation shock and reattachment point were simultaneously at their most upstream and downstream positions respectively, and vice versa. This suggested an expansion/contraction of the separation bubble, confirming the earlier laser Doppler velocimetry (LDV) work of Kussoy et al. [23]. Later work using the same configuration by Erengil & Dolling [24] showed that the separation shock was actually a system of compression waves near the wall, and that the motion of the separation shock was highly correlated with the pulsations of the separation bubble. Thus, it would seem that the separation bubble is responsible for driving the unsteady loading of closed SBLI.

The mean and unsteady pressure distributions from Gramann & Dolling [22] are displayed in Figure 5(a) and Figure 5(b), respectively. Note that in Figure 5 the abscissa is the streamwise coordinate x normalized by the incoming boundary layer thickness δ_0. The ramp corner lies at $x/\delta_0 = 0$, with the negative x-direction moving upstream through the interaction. In Figure 5(a), the ordinate is the time-averaged wall pressure at each station $\bar{p}_w$ normalized by the incoming boundary layer pressure p_∞. The flow is gradually compressed as it passes the point of upstream influence, which corresponds to the maximum upstream location of the separation shock foot. There is an inflection point in the mean pressure contour at the separation point S, followed by a substantially decreased pressure gradient across the

separation bubble, which can be attributed to the overhead free shear layer. This is followed by a significant increase in compression strength just before the reattachment location R, which continues until the inviscid pressure limit is reached on the ramp face some distance downstream.

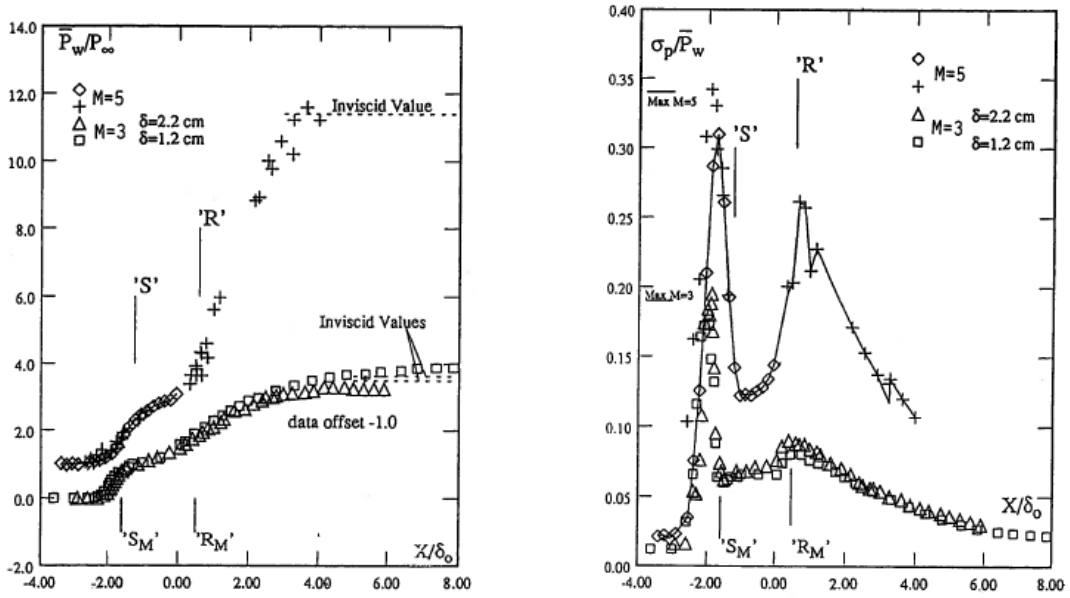

(a) (b)

Figure 5. Wall pressure distributions beneath a compression ramp SBLI, from Gramann & Dolling [22]. Figure adapted from Dolling [15]. (a) mean pressures (b) RMS pressures.

In Figure 5(b), the ordinate is the root-mean-square (RMS) deviation of the pressure signal at each station σ_p normalized by $\bar{p}_w$ at the same station over the time of interest. $\sigma_p/\bar{p}_w$ effectively describes the magnitude of unsteady loading at each location. As the flow traverses the interaction, there is a sharp increase in $\sigma_p/\bar{p}_w$ from the level caused by the passage of turbulent structures in the incoming boundary layer to a distinct maximum occurring very near S, which is due to the frequent passage of the separation shock foot. There is a momentary lapse in unsteady loading across the separation bubble followed by a second maximum near R.

Both of the local maxima in $\sigma_p/\bar{p}_w$ observed here are a result of the unsteady expansion and contraction of the separation bubble [15].

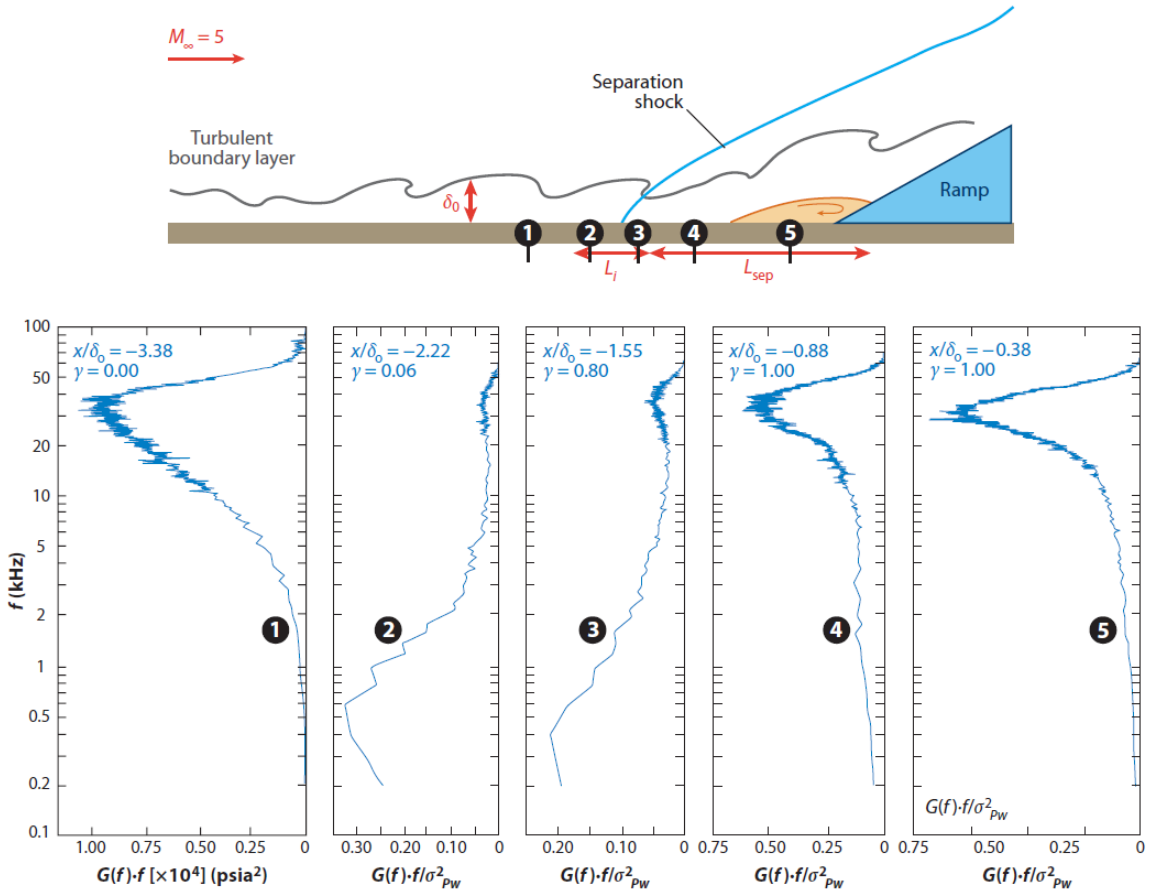

Figure 6. Power spectra of unsteady pressure loading beneath a compression ramp SBLI, from Gramann & Dolling [22]. Figure adapted from Clemens & Narayanaswamy [19].

The power spectra of the unsteady wall pressure loading beneath the 2D compression ramp SBLI of Gramann & Dolling [22] evolve from station to station as shown in Figure 6. The ordinate is the pressure signal frequency f, whereas the abscissa represents the premultiplied power spectra of the unsteady pressure at each station $G(f) \times (f)$ (note that at some stations $G(f) \times (f)$ is scaled by σ_p^2 for ease of comparison). The frequency content of

the incoming boundary layer at station 1 is distributed across a range from $\approx 10\,kHz - 50\,kHz$, with peak frequencies of approximately $40\,kHz$. This frequency range is again associated with the jitter of the passing turbulent boundary layer. The power spectra of stations 2 and 3 correspond to the motion of the separation shock foot across L_i, and are bimodal with dominant frequencies below $1\,kHz$. An example time-series of wall pressure below the intermittent region is shown in Figure 7, where two distinct pressure levels can be observed. The lower level signal from $t \approx 1 - 2\,ms$ is similar to that of the incoming turbulent boundary layer, whereas the occasional transitions to the higher level at $t \approx 2\,ms$ and back down at $t \approx 3\,ms$ are indicative of the intermittent passage of the separation shock foot. Downstream of the intermittent region, the flow at stations 4 and 5 loses the low frequency contribution from the separation shock unsteadiness and begins to resemble the incoming boundary layer. Near the downstream reattachment point on the ramp face (not shown here), the flow regains some low-frequency content from the flapping of the separation bubble that corresponds to the peak in $\sigma_p/\bar{p}_w$ at R in Figure 5(b).

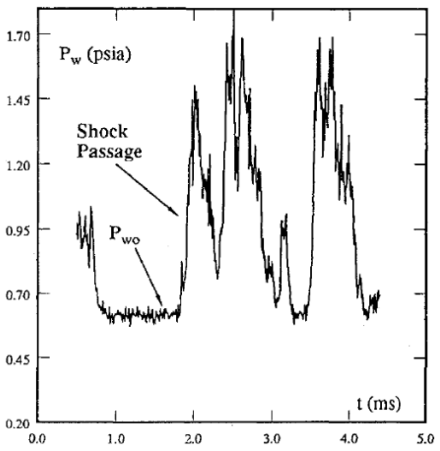

Figure 7. Wall pressure time series beneath intermittent region. Figure adapted from Erengil & Dolling [25].

In the context of inlet unstart, it is important to understand how the mean and unsteady features of 2D SBLI vary with the inviscid pressure ratio across the interaction, as this ratio will increase directly with the combustion-induced heat release in an engine. Dolling & Or [26] performed wall pressure measurement at the centerline of a 2D SBLI generated by a compression ramp of variable angle in a Mach 3 flow. The mean and unsteady pressure distributions over the range of compression angles tested are displayed in Figure 8(a) and Figure 8(b), respectively.

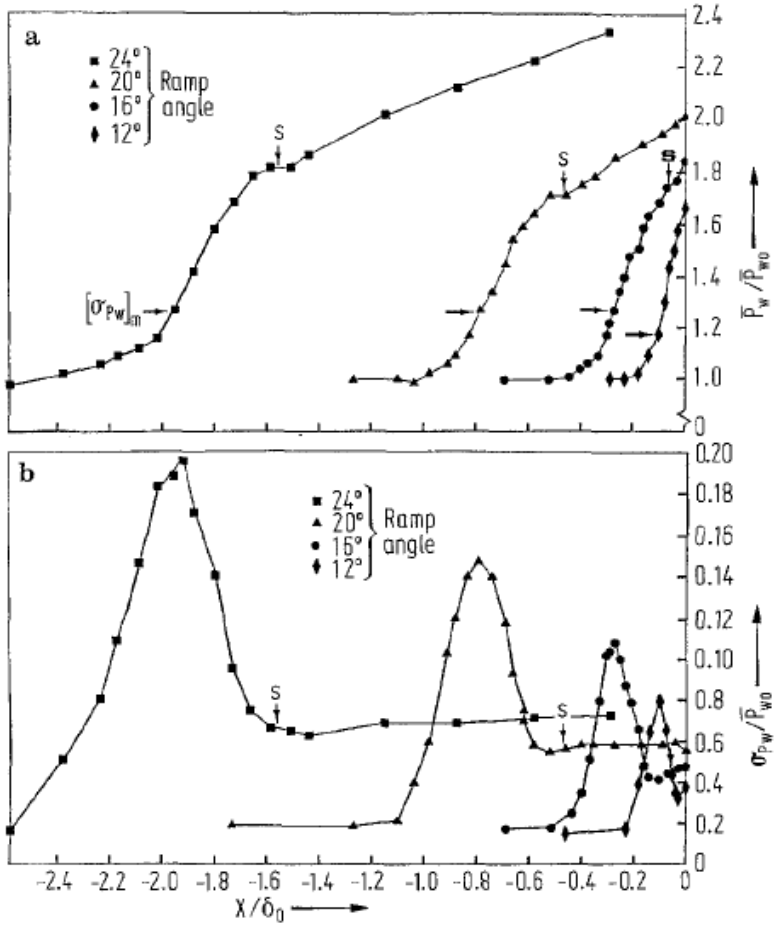

Figure 8. Wall pressure contours beneath a compression ramp SBLI with varying angle, from Dolling & Or [26]. (a) mean pressures (b) RMS pressures.

In general, the qualitative trends observed in Figure 8 are in agreement with those seen by Gramann & Dolling [22] for all ramp angles, although it should be noted that no measurements could be taken on the ramp face by Dolling & Or [26]. In general, an increase in ramp angle corresponds to an increase in the separated flow length scale L_{sep} due to the increased magnitude of the inviscid pressure ratio. Similarly, the low-frequency oscillation of the separation shock foot was seen to grow in power with increasing ramp angle, indicating a strengthening of the separation shock wave.

As discussed previously, the results here are somewhat limited in their relevance to rectangular inlets. However, they provide several key insights into the mean and unsteady nature of a portion of the unstart SBLI unit. They also introduce several key concepts, an understanding of which will prove useful in analyzing the similarities and differences between the 2D SBLI along the isolator floor and the highly complex interaction that takes place along the corner junction.

2. Three-dimensional shock boundary layer interactions

When considering the wealth of knowledge that has amassed in the area of 2D SBLI, comparatively few studies have focused on 3D SBLI. The majority of these efforts have been concentrated on swept compression ramps or glancing fin SBLI, with a few investigations into crossing planar shocks generated by sets of sharp fins [15]. Generally, the results of these studies are qualitatively similar to those of the 2D compression ramp case, although in the glancing fin interactions (and limited cases with significant compression ramp sweepback) quasi-conical symmetry is observed in the mean and unsteady pressure distributions extending

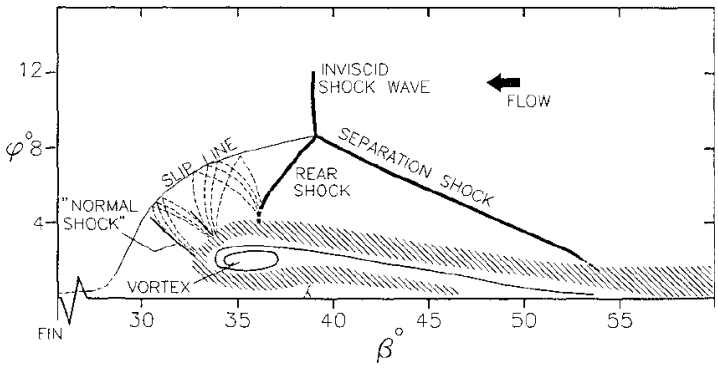

Figure 9. Flow features of a glancing fin SBLI. Figure adapted from Alvi & Settles [27].

outward from a virtual conical origin, or VCO [28, 29]. The flow structure of such an interaction is shown in Figure 9 in spherical coordinates. The near wall bifurcation of the glancing shock into a λ-structure is evident, with a streamwise separation vortex forming below the rear shock that entrains fluid and carries it downstream, hence the classification as an open SBLI mentioned previously [27]. Interestingly, a second peak in the $\sigma_p/\bar{p}_w$ curve (in addition to the one beneath the separation shock) is clearly apparent beneath the core of this vortex. While not the main focus of the present work, the glancing type interaction is of considerable importance in the isolator flowfield, particularly along the sidewalls [20].

Another relatively important portion of the unstart SBLI can also be classified as 3D. At the junctions of the inlet floor/ceiling and sidewalls, corner boundary layers are formed. The corner boundary layer exhibits several marked differences from the canonical 2D turbulent boundary layer. Davis et al. [30], who performed an experimental and numerical investigations of flow through a square duct at Mach 3.91, noted the formation of a streamwise vortex pair about the corner bisector, as depicted in Figure 10. These streamwise vortices grow with downstream distance as they entrain the inviscid core flow, resulting in an area blockage effect.

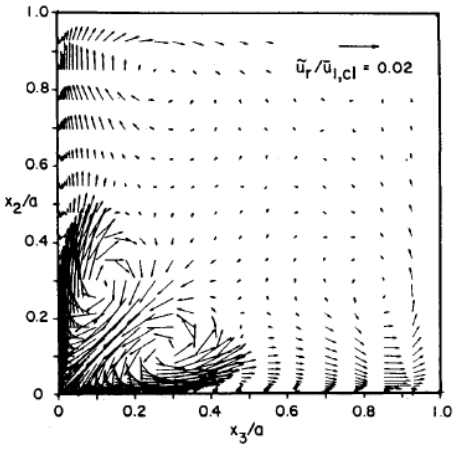

Figure 10. Corner vortex pair cross flow vectors. Figure adapted from Davis et al. [30].

Where the corner boundary layer meets the impinging/reflected shock in the isolator, a corner SBLI is formed. The qualitative nature of the corner SBLI has only been investigated relatively recently, with the bulk of the work taking place over the last six years. Burton et al. [31] and Bruce et al. [32] performed Schlieren imaging and surface streakline visualization in a normal shock SBLI in a rectangular duct at Mach 1.4 and Mach 1.5. The corner flow was modified via suction or blowing through slots in the floor upstream of the interaction. Blowing drastically increased the size of the corner separation observed, and resulted in a decrease in the extent of centerline (primary) separation observed. When suction was introduced, a reduced corner separation was seen but the primary separation increased considerably. The size of the λ-foot seen in the Schlieren images also increased with the size of the corner separation, leading to the development of the physical model depicted in Figure 11. The presence of two dominant, 3D corner vortices cause heavy, quasi-conical bifurcation of the normal shock wave in the corners, and increases the bifurcation at the centerline to a lesser extent. Static pressure measurements below the interactions at the centerline and corner confirmed this, with the

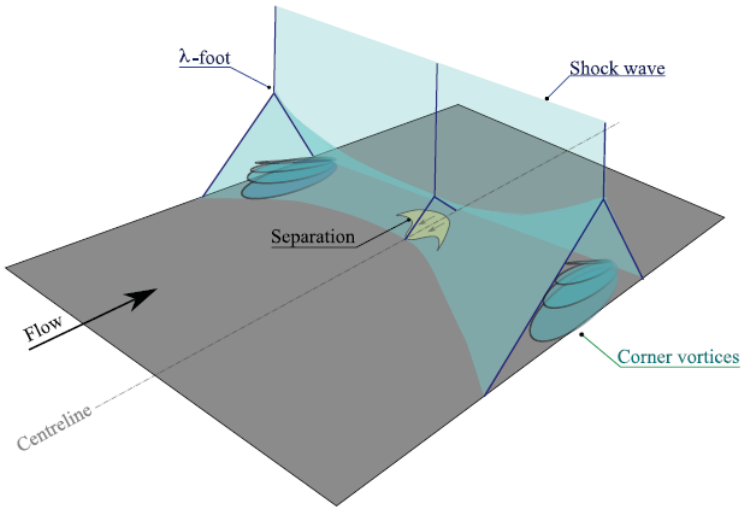

Figure 11. Physical model for corner SBLI induced bifurcation, from Burton et al. [31].

initial rise in $\bar{p}_w/p_\infty$ occurring farther upstream in the corner SBLI and with a lesser adverse pressure gradient when compared to the centerline. The cases with larger corner separations exaggerated the primary bifurcation effect, leading to a milder adverse pressure gradient along the centerline and the reduced separation mentioned previously. This shows that the corner SBLI can act to significantly modify the characteristics of the primary SBLI.

Conversely, Babinsky et al. [33] investigated the effects of corner separation in a Mach 2.5 impinging oblique SBLI in a rectangular channel. In this case the initial pressure rise along the corner again occurred upstream of the primary interaction due to the formation of corner shock waves. However, due to the swept nature of the impinging shock, when the corner separation size (and subsequently the strength of the corner shocks) was modified it was found that the corner shocks could intersect near the centerline upstream of the impinging shock, causing a stronger adverse pressure gradient and increased separation there. Thus, the corner SBLI is of importance in the shock trains of rectangular inlet/isolators, where it could act to

modify the primary impinging shock and precipitate the formation/strengthening of the unstart shock system. It is, therefore, desirable to gain a quantitative understanding of the mean and unsteady features of the corner SBLI itself and its driving mechanisms, about which relatively little is known.

The large-eddy simulations (LES) of Bisek [34] directly investigated the nature of the corner SBLI induced by a 24° compression ramp in a Mach 2.25 flow through a rectangular channel. A corner vortex similar to those seen in the aforementioned works was observed along the floor, although interestingly it was seen to coincide with the separation vortex of the glancing SBLI along the sidewall. The outflow plane of Figure 12(a) shows the wave structure of the swept interaction. The corner separation vortex was seen to entrain and eject fluid from the incoming corner boundary layer and from the separation beneath the primary shock front, as shown in Figure 12(b). Notably, the corner SBLI exhibited low frequency content similar to the unsteady characteristic motions of the previously discussed 2D SBLI. A possible

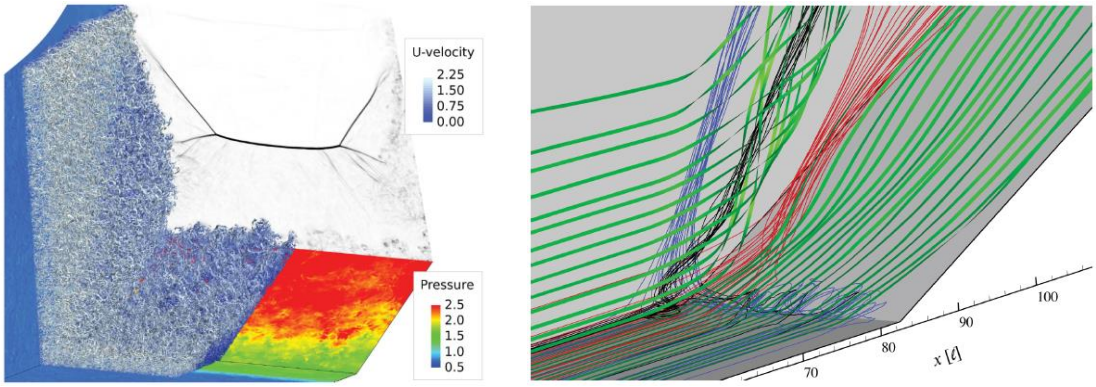

(a) (b)

Figure 12. Glancing sidewall interaction, from Bisek [34]. (a) Shock structure. Turbulent structures and pressure distribution also shown (b) velocity streamlines. Streamlines through corner vortex highlighted in black.

limitation of this study is the relatively low turbulent Reynolds number ($Re_\theta = 4300$), which is nearly an order of magnitude lower than those seen during unstart.

D. Motivation

The prior discourse shows that SBLI play an important role in the formation and propagation phases of rectangular inlet unstart, which is a serious issue plaguing the development of the next generation of hypersonic air-breathing vehicles. The main driving mechanism of unstart is the back pressure rise due to combustion-induced heat release, which results in the formation of the unstart shock system through the incipient separation of the isolator boundary layer.

The SBLI that comprise the unstart shock systems observed can be loosely grouped into the 2D interactions along the isolator floor and the 3D interactions along the sidewalls and corners. While the floor and glancing sidewall interactions are relatively well understood, much less is known about the corner SBLI. Few studies have attempted to classify its unsteady aspects, which could be of considerable importance in the transient unstart flowfield. In order to gain a more complete understanding of the physics of the unstart-specific SBLI, it is desirable to obtain both qualitative and quantitative measurements of the corner SBLI (and the companion primary SBLI) at reduced back pressure ratios similar to those seen in the aforementioned works. A subsequent analysis of the evolution of the trends developed there with increasing back pressure ratio may elucidate what role the primary and corner SBLI (as well as any interactions between them) play in the unstart process.

II. EXPERIMENTAL SETUP AND METHODOLOGY

A. Wind tunnel facility

All tests were performed in the North Carolina State University supersonic wind tunnel, shown in Figure 13. The NCSU tunnel is of the blowdown type with an oblique shock diffuser and a variable test section Mach number range from 1.75 to 4.5. The tunnel test section is of constant area measuring $150\,mm \times 150\,mm$ in cross section and is $650\,mm$ long. Experimental models are generally top mounted from a customizable plug in the tunnel ceiling. Test section access is provided through removable sidewalls that house quartz windows, which allow optical access during runs. A computer with a custom LabVIEW VI was used to control the length and settling chamber pressures of each run.

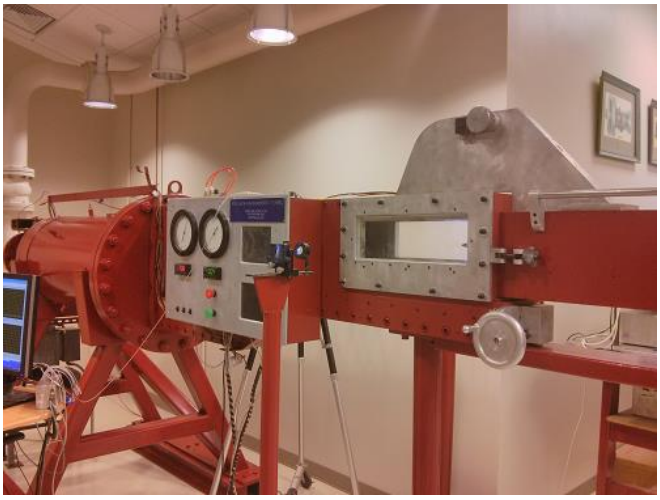

Figure 13. NCSU supersonic wind tunnel facility.

B. Freestream conditions

For the present study the freestream Mach number, M_∞, was fixed at 2.5. A PID controller was implemented and used to command a constant settling chamber pressure, p_{01},

of 80.7 psi for all tests. This yielded a nominal freestream pressure, p_∞, of 4.7 psi, calculated through the isentropic flow pressure ratio relation shown in Equation 1 (see Table 1 for a tabulation of freestream conditions). In Equation 1, γ is the ratio of specific heats for air.

$$\frac{p_{01}}{p_\infty} = \left[1 + \frac{\gamma - 1}{2} M_\infty^2\right]^{\frac{\gamma}{\gamma - 1}} \tag{1}$$

The settling chamber temperature, T_{01}, was maintained at 310 K. This corresponded to a freestream temperature, T_∞, of 138 K, calculated using the adiabatic temperature ratio displayed in Equation 2. This yielded a nominal freestream velocity, u_∞, of 589 m/s through the definition of the Mach number (Equation 3). Freestream velocity variations were estimated at $\pm 5\%$ or less from test to test.

$$\frac{T_{01}}{T_\infty} = 1 + \frac{\gamma - 1}{2} M_\infty^2 \tag{2}$$

$$u_\infty = M_\infty \sqrt{\gamma R T_\infty} \tag{3}$$

The freestream dynamic viscosity, μ_∞, was calculated using Sutherland's law with reference viscosity $\mu_{ref} = 1.719 \times 10^{-5} \frac{kg}{m\,s}$, reference temperature $T_{ref} = 273.15\,K$, and Sutherland's temperature $S = 110.4\,K$ as presented in Equation 4. The freestream density, ρ_∞, was calculated using the ideal gas law. This gave a unit Reynolds number, Re/L, of 5.1 $\times$ $10^7 m^{-1}$ (Equation 5).

$$\mu_\infty = \mu_{ref} \left(\frac{T_\infty}{T_{ref}}\right)^{\frac{3}{2}} \frac{T_{ref} + S}{T + S} \tag{4}$$

$$\frac{Re}{L} = \frac{\rho_\infty u_\infty}{\mu_\infty} \tag{5}$$

Table 1. Freestream test conditions.

Parameter	Value	
M_∞	2.5	
p_∞	4.7	psi
T_∞	138	K
ρ_∞	0.818	$\frac{kg}{m^3}$
u_∞	589	m/s
μ_∞	9.53×10^{-6}	$\frac{kg}{m\,s}$
Re/L	5.1×10^7	m^{-1}

C. Corner SBLI model

The experimental corner SBLI model developed and the classical SBLI coordinate system utilized are depicted in Figure 14. It consisted of a flat floor plate $370\ mm$ long and two sidewall fences made of carbon steel, forming a rectangular channel $70\ mm$ wide and $25\ mm$ in height. In Figure 14, note that the leading edges of the floor plate and sidewall fences tapered to sharp edges from the outside to avoid casting unwanted shock waves into the measurement domain. The model was mounted incident with the freestream flow and was lifted out of the ceiling boundary layer of the tunnel by two mounting struts, not shown here (for a complete description of the auxiliary experimental setup, see [35]). Along the floor plate, a 2D boundary layer formed and underwent a natural transition to turbulence. At the junctions of the floor plate and sidewalls, corner boundary layers were formed. The floor and corner boundary layers developed along the channel before interacting with the oblique shock generated by a downstream compression ramp, the angle of which was variable to allow for

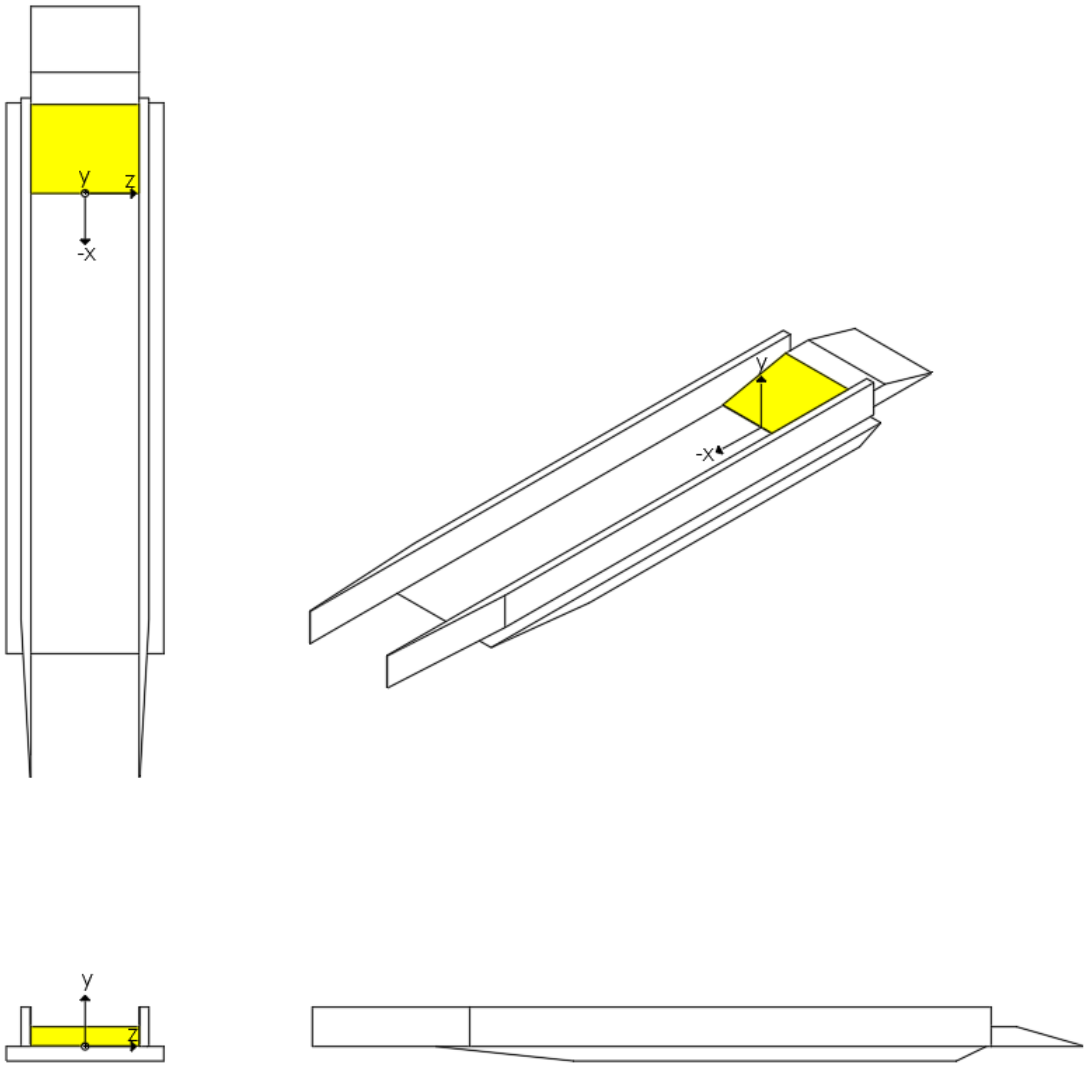

Figure 14. Three-view and isometric schematics of corner SBLI model. Coordinate system utilized also pictured, compression ramp face highlighted in yellow.

changes in the back pressure ratio between runs. The corner of the compression ramp was located 300 mm downstream of the leading edge of the floor plate for all tests. Table 2 shows the various ramp configurations and the corresponding inviscid back pressure ratios, p_b/p_∞, at $M_\infty = 2.5$. The choice in ramp angles follows from the work of Dolling & Or [26], who

Table 2. Ramp configurations and inviscid pressure ratios at $M_\infty = 2.5$.

Ramp angle	p_b/p_∞	% *N.S.R.*
12°	2.09	29.3
16°	2.60	36.5
20°	3.21	45.1
24°	3.94	55.3

reported a mean separation of 0.2δ in a Mach 3 flow at 12° and no separation below this angle. The inviscid pressure ratios in Table 2 are also shown as a percentage of the normal shock pressure ratio for the chosen freestream Mach number. Typically, unstart initiation occurs at around 70% of the normal shock ratio, and the ramp angles chosen span a range that is representative of a buildup to near this value from a relatively mild initial adverse pressure gradient. Again, it is important to note that the compression ramp angles were varied between test cases and not actively.

D. Experimental methods

1. Surface streakline visualization

To achieve a qualitative understanding of the mean flow features of the primary and corner SBLI, surface streakline visualizations were performed at each back pressure ratio. While the lifted nature of the 2D separation bubble and 3D topology of the corner SBLI make a volumetric measurement technique (such as particle image velocimetry) preferable to a surface tracer method, as of the time of this writing the infrastructure for such measurements in the NCSU supersonic tunnel is still under development. Two surface streakline visualization

types were utilized, the primary difference between the two being the speed at which the mixture dried.

The first type of streakline visualization consisted of a fast-drying mixture of aluminum oxide and kerosene oil, which was painted onto the model before starting the tunnel and allowed to set over the course of a run. In the interest of obtaining the best possible contrast with the white mixture, the model surfaces were painted flat black using latex enamel paint from Krylon, Inc. Images were recorded after tunnel shutdown and model removal, providing a time-averaged contour of regions of low wall shear stress. This aided in the identification of the separation regions and vortex patterns through the accumulation of pigment. Extents of low density regions, such as the corner boundary layer, could also be approximated using this medium. The model was top-mounted from the tunnel ceiling when using the fast-drying mixture, per the schematic shown in Figure 15. Test duration was limited to 5 *s* at the test

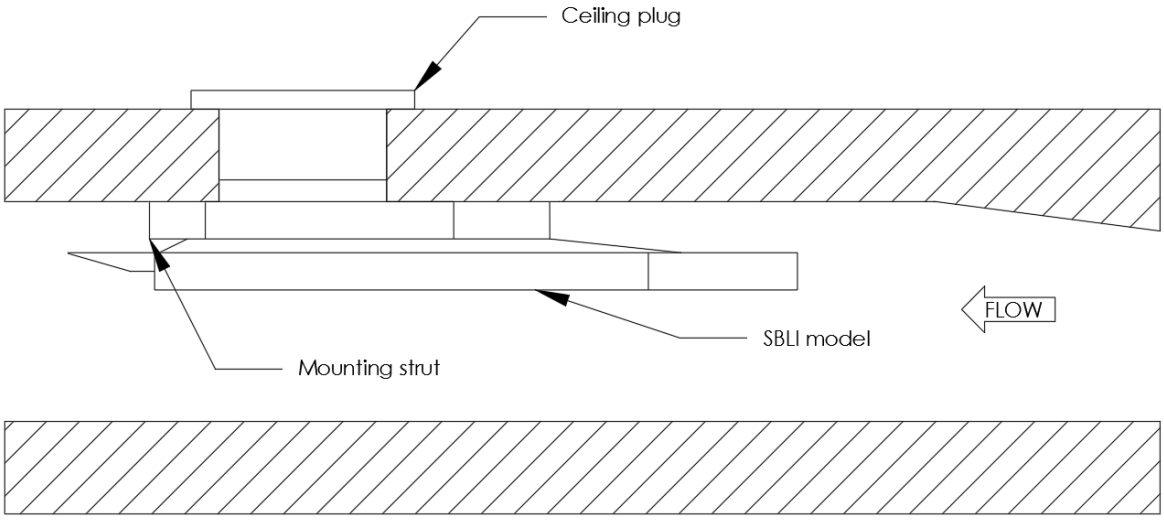

Figure 15. Side-view of top-mounted SBLI model.

Mach number to prevent the mixture from being blown away once dried.

The second streakline visualization method involved an extremely slow-drying mixture of mineral oil and DayGlo Rocket Red pigment, which fluoresces red when exposed to ultraviolet (UV) light. This combination of properties enabled unsteady imaging of the SBLI over the duration of a run using a JAI color CCD camera at a framerate of $60\ Hz$, with the field of view illuminated by a uvBeast UV LED flashlamp. The extreme viewing angles required to record the flowfield of the top-mounted model were impractical, necessitating the development of a secondary sidewall mount, as shown in Figure 16. It should be noted that the sidewall mounting method was unique to the unsteady streakline visualization, and all other testing methods utilized the top-mounting method. Unfortunately, any discrepancies in inflow conditions that arose from sidewall mounting could not be measured directly. However, it will

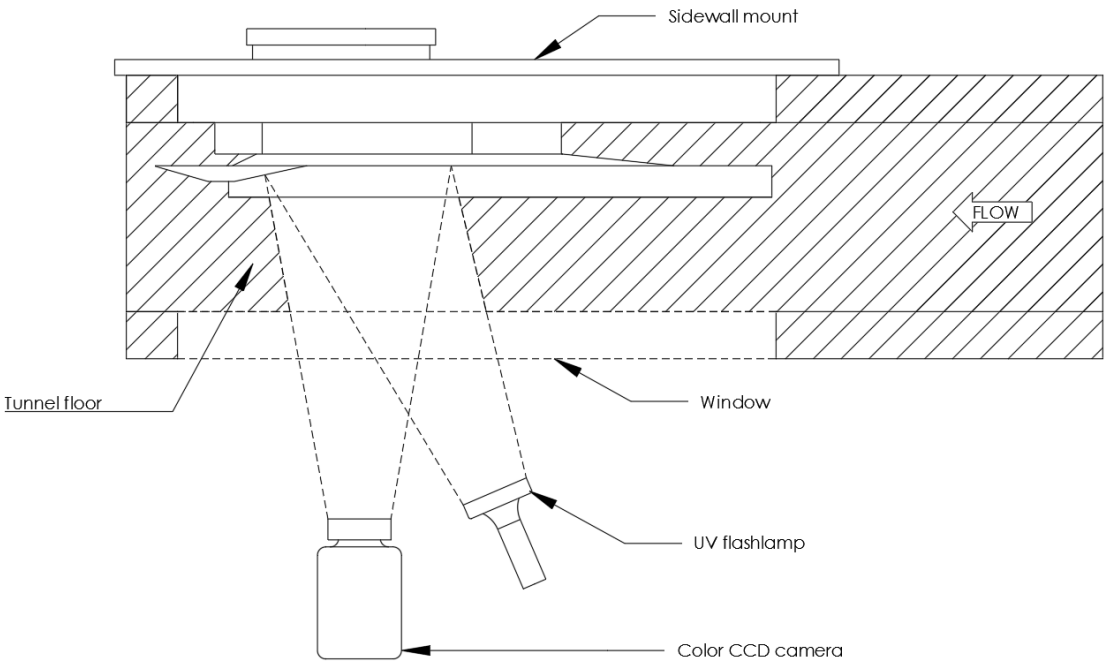

Figure 16. Top-view of sidewall-mounted SBLI model and unsteady surface streakline visualization setup.

be shown that the two streakline visualization methods generally show good agreement in terms of the mean flow structures observed and their extents; therefore, it is probable that the unsteady streakline visualization method provides an accurate picture of the mean flow kinematics and their evolution with increasing back pressure ratio. The approximate field of view on the SBLI model is depicted in Figure 16 (note the exclusion of the top sidewall fence for display purposes) and measured $70\,mm$ in the spanwise direction and $95\,mm$ in the streamwise direction. The upstream edge of the field of view laid approximately $60\,mm$ upstream of the compression ramp edge; this allowed for simultaneous imaging of the entire interaction along the floor plate and the downstream reattachment region along the ramp face over a test duration of $8\,s$. The streakline visualizations were also useful in that they aided in the placement of transducers for subsequent wall pressure measurements along the floor plate.

2. Wall pressure measurements

To gain a quantitative grasp on the mean and unsteady characteristics of the primary and corner SBLI and their evolutions with increasing back pressure ratio, high-frequency wall pressure measurements were performed. The transducer utilized was the high-frequency response Kulite Semiconductor Products, Inc. model XCQ062-15A. This sensor has a nominal diameter of $1.7\,mm$ and an effective frequency response of $50\,kHz$. It was mounted inside a bored-out #4-40 socket head cap screw using JB Weld epoxy steel resin, such that the transducer tip was flush with the tip of the screw. Tapped holes were machined in the floors of the experimental models such that the transducer tips were completely flush with the floor plate during the tests. The transducer leads ran out of the back of the model through shielding struts

that protected them from the open flow channel between the mounting struts. The leads then exited the tunnel through a hole in the ceiling plug, and ran to a ten channel Vishay Measurements model 2350 amplifier, which boosted each signal for increased resolution. Signals were subsequently low-passed at 25 kHz using a Stanford Research Systems SR600 low-pass filter before being digitized at a rate of 100 kHz using a National Instruments, Inc. model 9215 analog-to-digital converter and recorded using a LabVIEW VI. Error in the final pressure signals due to noise introduced by the electronics is estimated to be on the order of $\pm 3\%$.

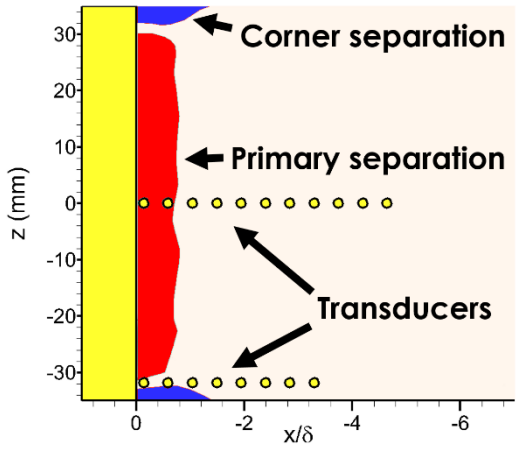

Figure 17. Top-down view of transducer positions relative to example flow features of interest and coordinate system utilized, compression ramp face highlighted in yellow. Figure adapted from Funderburk & Narayanaswamy [35].

A top-down view of the transducer positions relative to example flow features of interest is depicted in Figure 17, which also displays the coordinate system utilized. Note that the ramp face is highlighted in yellow and that the flow direction is from right to left. Sets of up to eight transducers could be placed in one of two spanwise rows, one coincident with the

channel centerline ($z = 0\,mm$) intended to measure the primary SBLI, and another at $z = -33\,mm$ beneath the corner interaction. The edge of the most downstream transducer in each row was coincident with the compression ramp leading edge, with subsequent transducers spaced every $4.5\,mm$ moving upstream. For all tests at least two transducers were located beneath the incoming boundary layer, with at least one transducer under the intermittent region and at least one transducer below the separated flow region. The transducer resolution could be artificially increased by shifting the leading edge of the ramp backwards by $\sim 2\,mm$ between runs, this effectively doubled the spatial resolution of the pressure profiles recorded. It should be noted that this does change the boundary layer development length entering the leading edge of the interaction, although any effects arising from the additional $2\,mm$ on the mean pressure profiles are considered to be negligible. However, an important caveat does arise with respect to the two-point cross-coherences utilized, in that the two pressure signals must be taken from the same test. Therefore, the minimum distance between cross-coherence stations was limited to $4.5\,mm$.

An in-house MATLAB code was developed and used for the processing of the wall pressure signals. The mean and RMS wall pressure profiles were computed by taking an average and standard deviation of the pressure signals of each transducer for a given test over a $2\,s$ period where the rolling standard deviation of the wall pressure in the incoming boundary layer was less than 5%. The subsequent power spectral densities were computed over this $2\,s$ time period using Welch's method of windowed Fourier transforms [36], with a window size of 5000 samples and 50% overlap between windows. Cross-coherences were then performed

between two transducers (for the purposes of this explanation, they are denoted as transducers x and y) per Equation 6.

$$Coh(x,y) = \frac{\left|G_{xy}(f)\right|^2}{G_x(f)\, G_y(f)} \tag{6}$$

In Equation 6, $Coh(x,y)$ is the magnitude of the cross-coherence between the pressure signals from the two transducers, $G_{xy}(f)$ is the cross-spectral density of the two signals, and $G_x(f)$ and $G_y(f)$ are the power spectral density functions of the pressure signals of individual transducers x and y determined using the method discussed previously. The cross-coherence spectrum relates to the degree of coupling between the two pressure signals for a given frequency. While a cross-coherence magnitude of unity at a given frequency corresponds to a linearly coupled system at that frequency, a magnitude of zero corresponds to a completely uncoupled system.

III. INFLOW CHARACTERIZATION

A. Boundary layer measurement setup

The features of the incoming flow are critical factors in SBLI. Therefore, it was necessary to characterize the boundary layer near the streamwise interaction location without a compression ramp present before the interaction itself could be studied. Furthermore, an understanding of any pre-interaction modification to the floor inflow through the introduction of the sidewall fences and corner boundary layers was also key in the interpretation of test results. Two boundary layer profiles were obtained in the interest of meeting these criteria,

corresponding to the incoming flow at the quarter-span and centerline of the corner SBLI model.

Boundary layer profiles were attained through floor-normal pitot sweeps at two spanwise positions. The pitot probe utilized was custom-manufactured for the purposes of these tests, and is depicted in Figure 18. It consisted of a hollow steel stem, $6.3\ mm$ in diameter with a wall thickness of $0.9\ mm$. The wall of the stem was tapped at one end for a bored-out #0-80 screw, which tapered at the upstream end to the diameter of a small stainless steel tube that formed the pitot tip. The tip was located approximately $50\ mm$ upstream of the stem and had an orifice diameter of $0.25\ mm$, allowing the boundary layer profiles to be resolved with good spatial accuracy. A wedge was affixed to the leading edge of the stem along its length which generated an oblique shock, mitigating any interference associated with the standoff of

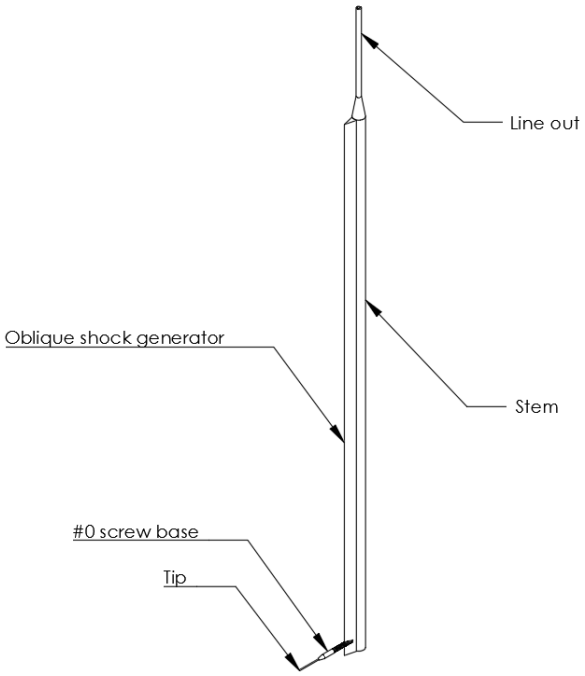

Figure 18. Custom-manufactured pitot probe for boundary layer profile measurements.

a bow shock from the blunt cylinder. The screw/stem and screw/tip junctions were sealed with epoxy steel resin, as were the tops and bottoms of the stem. The top of the stem narrowed to another stainless steel tube to which a pressure line was connected. Generally speaking, a considerable loss of frequency response was anticipated considering the voluminous cavity within the stem and the outgoing pressure tubing. This was not problematic for the boundary layer profiles, however, as they only considered the average stagnation pressures that developed at the test Mach number.

A special floor plate for the test article was developed, including slotted holes that allowed the stem of the custom pitot to pass through them, as depicted in Figure 19. Much like

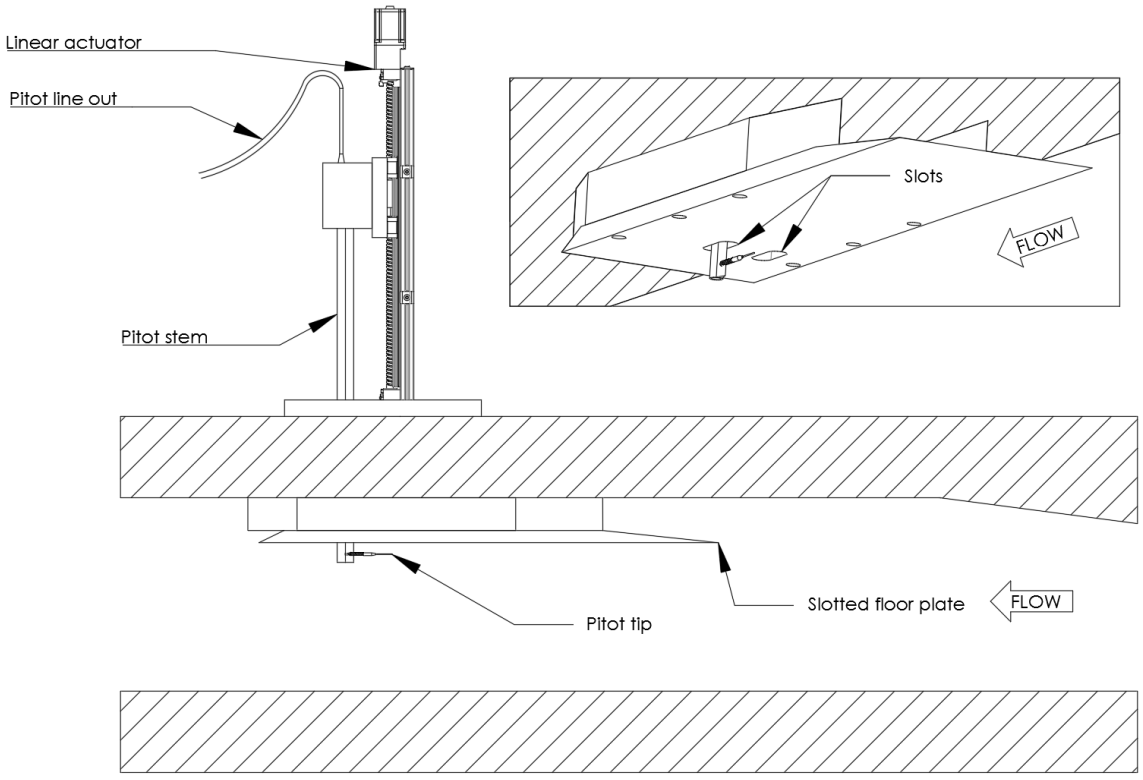

Figure 19. Boundary layer profile measurement setup. Note the exclusion of sidewall fences for display purposes.

the aforementioned transducer leads, the cylindrical pitot stem passed through a shielding strut before leaving the tunnel through a hole in the ceiling plug, where it was held in place by a Newmark Elements linear actuator. The linear actuator position was controlled by a computer and used to vary the floor-normal height of the probe from run to run with precision. The pressure line from the top of the pitot tube ran to a Kulite Semiconductor Products, Inc. model ITQ-1000-100A transducer. The signal was subsequently amplified before being digitized at a rate of $200\ Hz$ and recorded.

B. Boundary layer profile methodology

Pitot sweeps were performed at the centerline ($z = 0\ mm$) and quarter span ($z = -17.5\ mm$) locations of the corner SBLI model, approximately $50\ mm$ upstream of the nominal streamwise ramp corner position. Due to tunnel constraints, measurements could not be taken within the corner boundary layer. The sweeps began outside the boundary layer edge at $y = 12\ mm$, moving inwards toward the floor to a height of $y = 4\ mm$ in increments of $1\ mm$. Subsequent steps toward the plate surface were taken in increments of $0.5\ mm$ to refine the near wall profile. One test was performed at each height, with durations of $5\ s$ at the test Mach number of 2.5.

Time-correlated settling chamber and pitot pressure signals were recorded simultaneously over the course of each run. To obtain the subsequent velocity profiles, the methodology utilized was as follows. First, the settling chamber and pitot pressure profiles were averaged over a $1\ s$ period where the rolling standard deviation of both was less than 5%. Next, in the portions of the profile away from the wall where the pitot pressure remained

relatively constant with height, the average settling chamber and pitot pressure values for each run were substituted into the normal shock jump relation for stagnation pressures (Equation 7) as p_{01} and p_{02}, respectively. This relation could then be solved iteratively for M_1, the Mach number inbound to the pitot probe (upstream of the pitot bow shock) assuming the incoming flow was isentropic.

$$\frac{p_{02}}{p_{01}} = \left[\frac{(\gamma+1)M_1^2}{(\gamma-1)M_1^2+2}\right]^{\frac{\gamma}{\gamma-1}} \left[\frac{\gamma+1}{2\gamma M_1^2-(\gamma-1)}\right]^{\frac{1}{\gamma-1}} \tag{7}$$

In the lower regions of the profile where the boundary layer began to introduce stagnation pressure losses, the average settling chamber pressure was first substituted into the isentropic pressure ratio relation (Equation 1) as p_{01}, which was then solved to give p_1, the incoming boundary layer static pressure at $M_\infty = 2.5$. The normal shock relation for incoming static pressure and outgoing stagnation pressure was then used to solve for the inflow Mach number at the given height per Equation 8, assuming that the boundary layer pressure remained constant.

$$\frac{p_{02}}{p_1} = \frac{\left[\frac{(\gamma+1)M_1^2}{2}\right]^{\frac{\gamma}{\gamma-1}}}{\left[\left(\frac{2\gamma M_1^2}{\gamma+1}\right)-\left(\frac{\gamma-1}{\gamma+1}\right)\right]^{\frac{1}{\gamma-1}}} \tag{8}$$

The Mach number at each height and the upstream stagnation temperature, T_{01}, were substituted into the adiabatic temperature relation (Equation 2) to solve for T_1, the static

temperature inbound to the normal shock. This value was then substituted into Equation 3 to find the incoming velocity u_1 at each height.

Once a complete boundary layer profile was obtained, the compressible displacement thickness δ^* and momentum thickness θ were calculated by a trapezoidal integration of Equation 9 and Equation 10 from the floor plate to the edge of the velocity deficit ($\delta_{99\%}$). Note that the boundary layer profiles were refined below $y = 0.5\ mm$ using the method described by Sun & Childs [37] prior to integration.

$$\delta^* = \int_0^{\delta_{99\%}} \frac{\rho_1(y)}{\rho_\infty}\left(1 - \frac{u_1(y)}{u_\infty}\right) dy \tag{9}$$

$$\theta = \int_0^{\delta_{99\%}} \frac{\rho_1(y)u_1(y)}{\rho_\infty u_\infty}\left(1 - \frac{u_1(y)}{u_\infty}\right) dy \tag{10}$$

The momentum thickness was then substituted into Equation 5 to determine Re_θ. Finally, the boundary layer shape factor, H, was calculated using Equation 11.

$$H = \frac{\delta^*}{\theta} \tag{11}$$

C. Boundary layer profiles and channel surface streakline visualization

The results of the quarter-span and centerline pitot sweeps above the streamwise interaction location of the corner SBLI model are depicted in Figure 20, where the ordinate is the wall-normal height of the pitot probe y, and u_1 is the streamwise velocity at each height calculated using the aforementioned methodology. From Figure 20, it is evident that there is a

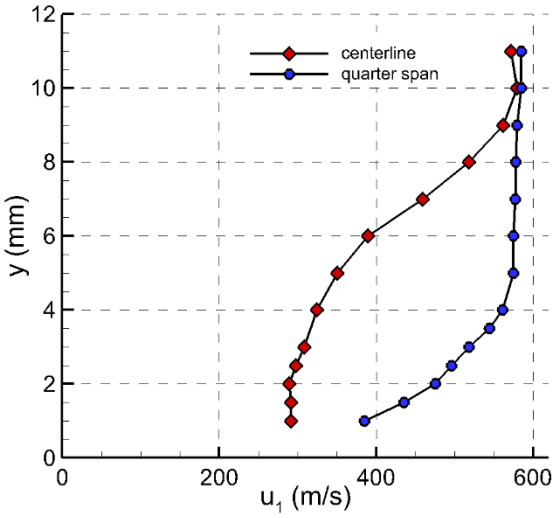

Figure 20. Corner SBLI boundary layer profiles at centerline and quarter-span of corner SBLI model with compression ramp removed.

distinct difference in the fullness of the boundary layer at the two spanwise locations. The boundary layer velocity thickness varies from $\delta_{99\%} \approx 5\,mm$ at the quarter-span to $\delta_{99\%} \approx 10\,mm$ at the centerline, indicating a significant velocity deficit in the lower regions of the centerline boundary layer. The centerline boundary layer profile also shows a distinct inflection point near the wall, which is characteristic of development through an adverse pressure gradient. As both spanwise locations were sufficiently displaced from the sidewall, little to no spanwise boundary layer variation was expected, and a subsequent explanation for this effect was desired.

To this end, an unsteady streakline visualization was performed along the entire length of the corner SBLI model with the compression ramp removed. Due to camera and lighting limitations two separate runs were performed with fields of view that overlapped slightly, as shown in Figure 21 and Figure 22. For these images (and all subsequent streakline

visualization) the flow is from right to left and the abscissa is normalized by the centerline boundary layer thickness of $10\,mm$, as discerned from Figure 20. In the interest of saving space, $\delta_{99\%}$ is abbreviated to δ for all subsequent figures and discussion.

For the upstream portion of the surface streakline visualization shown in Figure 21(a), the right edge of the image is coincident with the leading edge of the floor plate. The upstream edge of the image is relatively dark as the visualization mixture is swept away from the leading edge immediately upon the start of a test. Moving downstream, two transverse compression waves are visible that move toward the centerline from the top and bottom of the image (Figure 21(b) gives an approximation of the wave paths). The waves intersect around $z \approx 0\,mm$, $x/\delta \approx -26$, resulting in an increase in the pigment density and a subsequent improvement in signal. The wave angle is approximately $25°$ when measured from the bottom sidewall, which is very close to the Mach angle of the freestream flow ($\mu = 23.6°$). The compression waves also form some distance upstream of the leading edge of the floor plate, and it can subsequently be concluded that they emanate from the leading edge of either sidewall fence. As they intersect very near the centerline, they are not likely to be yaw-induced. They are initially very faint, and the flow along the floor plate does not turn visibly as it passes through them, indicating that these waves are not of substantial strength near the floor. They impinge on the opposite sidewall near $x/\delta \approx -19.5$ before reflecting more steeply just upstream of a transverse wave that spans the channel near $x/\delta \approx -18.5$. This shock is thought to form along the upstream edge of the window opposite the sidewall-mounted SBLI model, impinging on the open flowfield. While the floor flow in Figure 21 does turn as it passes through this wave, no such shocks are evident in Schlieren images of the top mounted model; therefore any effect of this

wave is negligible in all other tests. It is interesting to note that the corner boundary layers thicken very near the location of this impinging shock as evidenced by dark bulges in the top and bottom corner junctions.

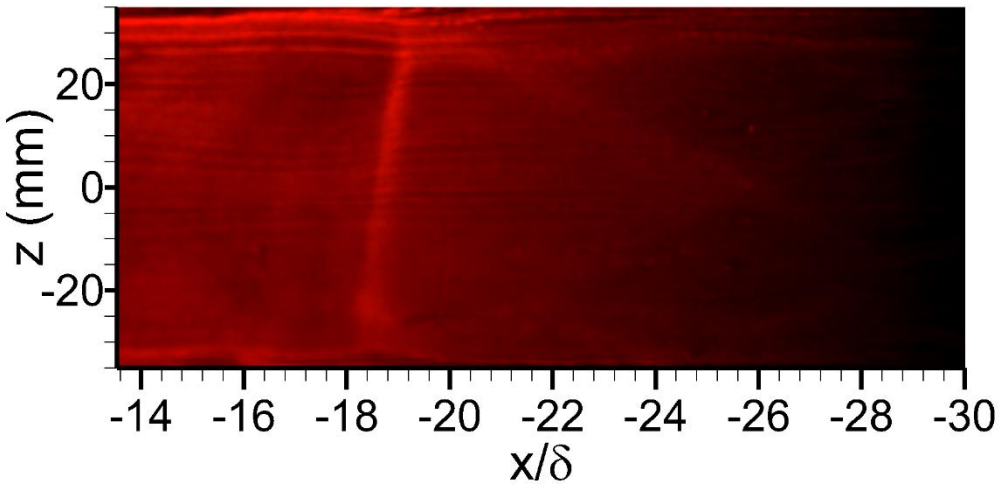

(a)

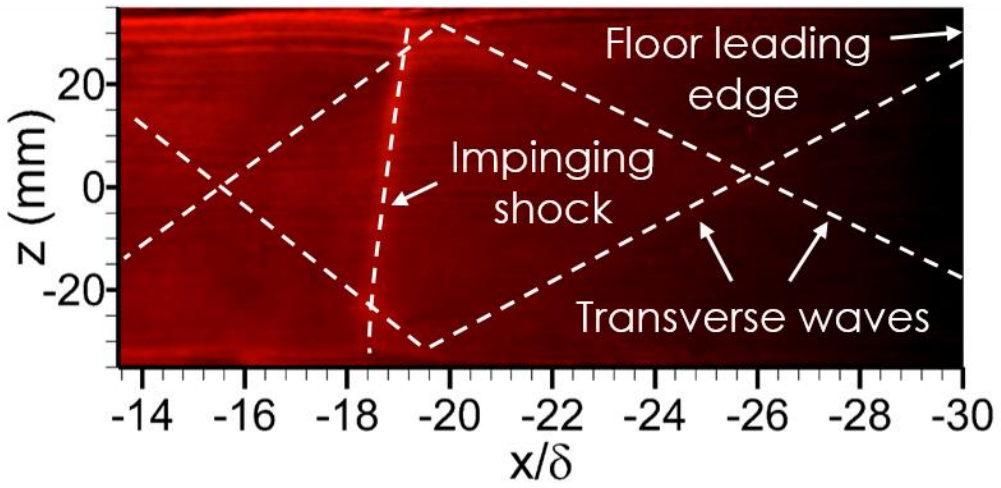

(b)

Figure 21. Unsteady surface streakline visualization of corner SBLI model with compression ramp removed, upstream field of view. (a) original image (b) annotated image.

However, as the thickening begins upstream of the impinging shock by nearly a full boundary layer thickness, it is expected that the first transverse shock reflection is the causal mechanism rather than the impinging window-wave.

As the flow moves into the downstream field of view shown in Figure 22, the transverse waves remain visible, reflecting for a second time near $x/\delta \approx -10$. The wave angle steepens noticeably through the reflection, and the corner boundary layers begin to thicken considerably in response, as evidenced by the dark bands bounded by a solid white line in Figure 22(b). This results in a slight area blockage effect near the floor as the flow approaches the nominal ramp leading edge location at $x/\delta = 0$. As the flow along the floor plate passes through the transverse waves downstream of the second reflection, it deflects considerably toward the centerline. This effect is probably due to decreased Mach number in the near-wall vicinity attributable to repeated processing of the floor boundary layer by the transverse waves, although at present no velocity measurements are possible upstream of the pitot tip locations (denoted by two yellow circles in Figure 22(b)) to examine the effect of the individual waves. It is interesting to note that at the location of the centerline pitot sweep ($z \approx 0\,mm$, $x/\delta \approx -5$), the incoming boundary layer has just been processed by the third transverse shock intersection; at the same streamwise location the quarter-span boundary layer has effectively navigated through one less wave and has traveled approximately 3δ since its most recent processing. At present, the transverse shock reflections are suspected as the cause of the centerline boundary layer velocity deficit. The presence of these waves cannot be assumed to be trivial; it is important to note that any modification to the incoming boundary layer of the compression ramp SBLI could have effects on the observed results. It is interesting to note that

Bisek [34] also observed traverse waves that emanated from the sidewall which persisted into the measurement domain, although the boundary layer profiles of the LES study were not affected to the degree observed here.

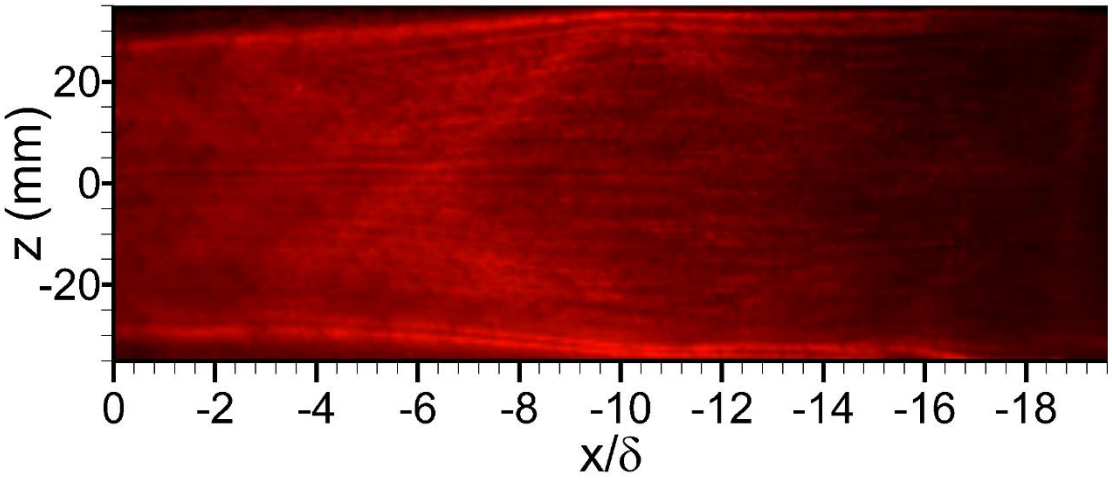

(a)

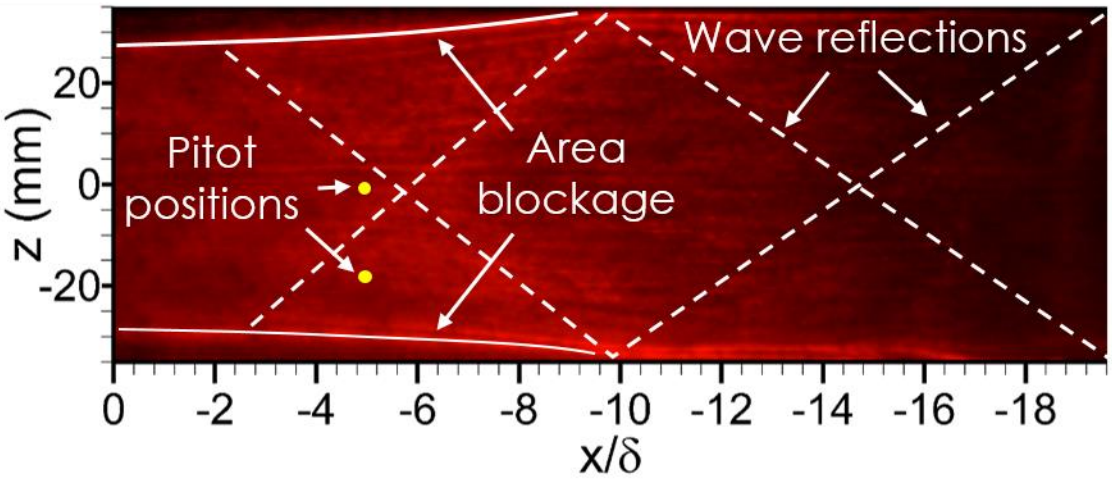

(b)

Figure 22. Unsteady surface streakline visualization of corner SBLI model with compression ramp removed, downstream field of view. (a) original image (b) annotated image.

As the spanwise differences in the boundary layer velocity measurements of Figure 20 cannot be discounted at present, two sets of boundary layer characteristics (shown in Table 3) were calculated using both the centerline and quarter span profiles. When the shape factors of the two profiles in Table 3 are compared, it is evident that the centerline boundary layer is subjected to a greater adverse pressure gradient. The momentum and displacement thicknesses of the centerline boundary layer are also considerably larger, which affects Re_θ in a similar manner. However, it will be shown that the separation lengths observed in the primary SBLI agree well with those of canonical 2D SBLI when normalized by the centerline boundary layer thickness. Conversely, normalization of the separation lengths using the quarter-span thickness generally returns results which are considerably larger than those seen in literature (even when the SBLI itself remains 2D). Therefore, the centerline boundary layer characteristics are considered to be more representative of the flowfield, yielding an Re_θ of 47500 for the study.

Table 3. Boundary layer characteristics at centerline and quarter-span of corner SBLI model with compression ramp removed.

Parameter	Centerline		Quarter-span	
$\delta_{99\%}$	10	mm	5	mm
δ^*	1.5	mm	0.26	mm
θ	0.93	mm	0.22	mm
H	1.61		1.17	
Re_θ	47500		11500	

IV. RESULTS AND DISCUSSION

The experimental results discussed here are presented in a manner that reflects the evolution of a rectangular inlet unstart event; first, the primary and corner SBLI are investigated for the mildest back pressure ratio case with a $12°$ compression ramp, with

subsequent analysis focusing on the development of the trends observed in the mild case with increasing compression strength for ramp angles of 16°, 20°, and 24°. This methodology is comparable to observing the formation and strengthening of the unstart shock system prior to the upstream propagation phase.

It should be noted that the results herein closely follow results presented in several works of the present author [38, 39, 40]. While several new conclusions and supporting evidence are presented, most of the results and the global conclusions reached remain the same.

A. Mild back pressure baseline

1. Surface streakline visualization

a. Time-averaged streakline visualization method

Figure 23 depicts several views of time-averaged streakline visualizations for the 12° ramp configuration. The junction of the sidewall and floor plate in the positive spanwise

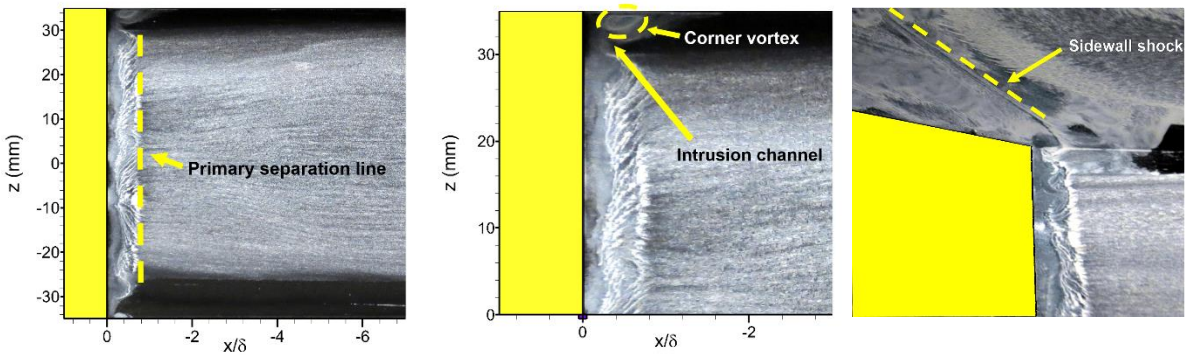

(a) (b) (c)

Figure 23. Time-averaged surface streakline visualization for 12° compression ramp configuration. Figure adapted from Funderburk & Narayanaswamy [38]. (a) annotated full-span top view (b) annotated semi-span top view (c) annotated sidewall view.

direction ($z > 0\,mm$) is referred to as the top corner, while the junction in the negative spanwise direction is referred to as the bottom corner. In Figure 23(a), the junction regions are rendered as dark bands. This may occur due to transverse fluid migration towards the centerline due to the aforementioned junction boundary layer blockage. A fairly symmetric growth of the corner boundary layer emanating from the two sides can be observed. While the surface streakline visualization does not provide an exact measure of the junction boundary layer thickness, the extent of the dark band does provide a lower bound estimate of the junction boundary layer thickness within a certain error margin. With this caveat, the extent of the corner boundary along the z-direction (spanwise direction of the floor plate) is approximately $10\,mm$ at the streamwise location just upstream of the ramp-induced separation.

Figure 23(a) and Figure 23(b) show the primary and corner separation boundaries that are discerned from the streakline visualization as dashed lines. The primary separation line can be visualized as the narrow band with a distinct brightness due to accumulation of the pigment mixture. The separation line is fairly straight over bulk of the spanwise region about the centerline ($-25\,mm < z < 25\,mm$), which indicates that the primary separation is two-dimensional along most of the span. In contrast, the separation line becomes highly curved as the top corner is approached in Figure 23(b) ($z > 30\,mm$). The footprint of a vortex structure is also evident in the top corner of Figure 23(b) from $z \approx 31 - 34\,mm$ and $x/\delta \approx -0.3$ to -0.8. Similar corner vortices were a salient feature in the previously described shock/corner boundary layer interactions of Burton et al. [31] and Burton & Babinsky [41], and also in the LES of Bisek [34]. The presence of the corner vortex structure here is significant and a strong indication that the flow structure of corner SBLI is 3D in the mean. This revelation

is important, as even in experiments with vortex generators placed upstream of impinging normal SBLI [42, 43], the injection of streamwise vortices (which are similar to those seen in the incoming junction boundary layer of the corner SBLI [30]) into the primary SBLI does not result in the formation of these highly 3D structures. This key dissimilarity suggests that the fundamental physics of the corner SBLI may differ from those of canonical 2D SBLI, and further investigation into the corner SBLI is likely necessary to fully grasp the unstart issue. The corner separation region also appears to be highly swept, and while it extends upstream of the primary separation line nearest the sidewall, it quickly recedes downstream a short distance away from it. This swept pattern agrees with the quasi-conical nature of the corner SBLI suggested by Burton et al. [31]. An intrusion "channel" is also evident in Figure 23(b) which separates the primary and corner separations. The separation extent near the intrusion channel is considerably less than that of the primary and corner separations. Bisek [34] argued that these channels form due to conical compression waves that emanate from the leading separation point of the corner SBLI, causing the nearby boundary layer to develop a slightly fuller velocity profile which delays the onset of separation.

Figure 23(c) depicts a separate streakline visualization run with a painted sidewall, and provides a clear picture of sidewall separation. It can be observed that the glancing oblique shock along the sidewall is initially curved in the region of the corner separation and recovers to a straight geometry within $1/6th$ of the fence height. The shock angle corresponds approximately to the inviscid value associated with the ramp angle and freestream Mach number. This suggests that the fence extends a significantly longer wall-normal height than the corner separation. Hence, the effects of spillage across the fence on the corner separation

features are expected to be minimal. Unfortunately, the quality of the visualization is not sufficient to provide details of the flow features associated with the sidewall separation.

b. Unsteady streakline visualization method

Figure 24 displays a snapshot from an unsteady streakline visualization of the 12° compression ramp flowfield. In general, the flow features observed agree well with those seen in the time-averaged case of Figure 23. The primary separation shape is nominally identical, and the aforementioned intrusion channel is also evident. While the corner vortices are not as easily discernable, the direction of their rotation near the floor can be determined from the outermost streakline that they entrain, which is highlighted in Figure 24. The rotational direction of the corner vortices agrees with the LES work of Wang et al. [20], as well as the rotational direction of the separation vortex beneath the glancing SBLI of Alvi & Settles [27].

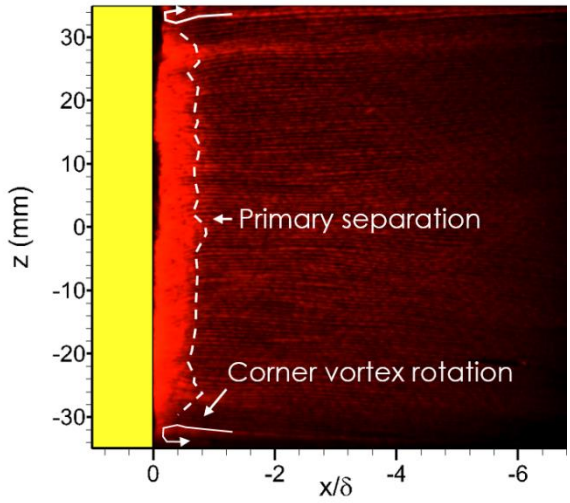

Figure 24. Annotated full-span top view of unsteady streakline visualization for 12° compression ramp configuration.

This would seem to strengthen the aforementioned supposition of Bisek [34], who claimed that the corner vortex is actually the separation vortex of the glancing sidewall interaction. The transverse shock intersection discussed previously is also faintly evident in the upstream portion of the image, and seems to have little to no effect on the two-dimensionality of the primary SBLI at this back pressure ratio.

2. Wall pressure measurements

a. Mean and RMS pressure profiles

Figure 25 shows the mean and RMS wall pressure profiles obtained within the primary and corner SBLI for the mildest back pressure ratio case. The average values from three datasets over separate experimental runs are shown. The mean wall static pressures at each transducer position are normalized by the freestream static pressure in Figure 25(a). Error bars were added to indicate the (two-sided) 99 percent confidence interval. Figure 25(a) indicates a clear rise in the wall static pressure from the freestream value in both the primary and corner SBLI as the compression ramp edge is approached. At $x/\delta \approx -1$, the wall static pressure in the primary SBLI increases above the freestream value and continues to rise to a value of $\bar{p}_w/p_\infty = 1.51$ at the most downstream measurement location ($x/\delta = -0.15$). Both the streamwise location of the initial pressure rise and the normalized wall static pressure nearest the compression corner agree well with values previously reported in 2D SBLI at a similar Mach number [26, 44]. The trends exhibited in the corner SBLI are largely similar to primary SBLI. However, it should be noted that the pressure increase along the corner separation is

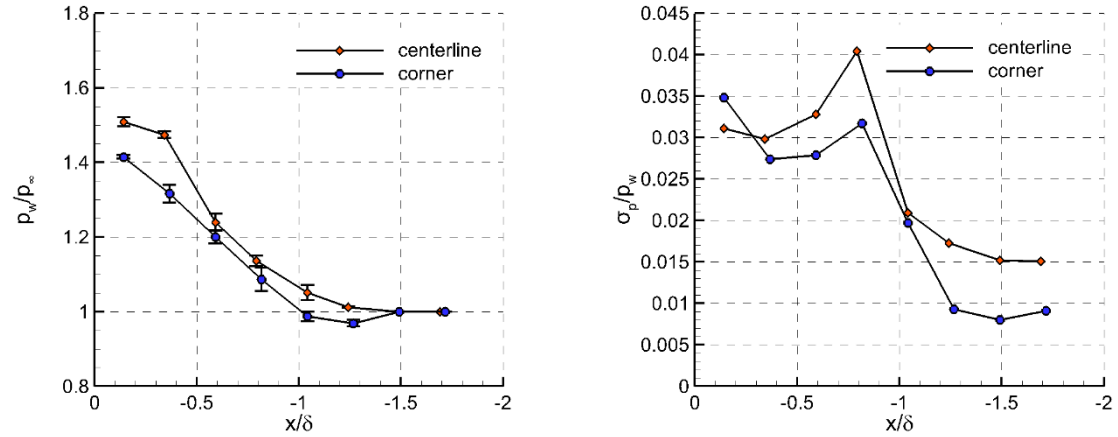

Figure 25. Wall pressure profiles for 12° compression ramp configuration. (a) mean pressures (b) RMS pressures.

consistently lower than in the primary separation for any given streamwise location by as much as $\bar{p}_w/p_\infty = 0.16$ (11%). This indicates a smearing of the adverse pressure gradient in the corner, a finding again consistent with those in transonic normal shock SBLI [41]. The smearing may be due to the presence of the corner vortex structure, which would be likely to cause a local decrease in static pressure. It should be noted that neither pressure rise approaches the inviscid limit ($p_b/p_\infty = 2.09$) estimated in Table 2; in fact, the remaining pressure rise is only attained at the downstream reattachment point, although no measurements could be taken on the ramp face with the present configuration.

The streamwise evolutions of the RMS pressures for the primary and corner SBLI for the 12° compression ramp case are shown in Figure 25(b). In the primary SBLI, it can be observed that there is an increase in pressure fluctuation as the flow moves downstream, starting from an initial value of $\sigma_p/\bar{p}_w = 0.015$ in the incoming boundary layer, to a peak of

$\sigma_p/\bar{p}_w = 0.040$ at $x/\delta = -0.8$, which corresponds to the intermittent region (vicinity of separation shock foot oscillations). Downstream of the intermittent region, there is a momentary decrease in pressure fluctuation within the separated flow, followed by an increase at the location closest to the compression ramp. The compilation of comparable RMS pressure profiles in 2D SBLI by Dolling & Or [26] shows very similar increasing trends as the intermittent region is approached, followed by the same decrease downstream. Interestingly, the pressure profiles for 12° there also exhibited an increase in $\sigma_p/\bar{p}_w$ just upstream of the compression ramp edge, as observed in the present results. Further, the peak normalized RMS pressure value falls between the values obtained at $M = 2.8$ by Dolling & Or [26] and $M = 1.5$ by Thomas et al. [45]. Therefore, the RMS pressure trends exhibited by the primary SBLI are also highly consistent with those of 2D SBLI [15].

Considering the normalized RMS pressure trends in the corner SBLI, it can be observed from Figure 25(b) that the magnitude of the normalized RMS pressure in the incoming corner boundary layer is smaller than that of the primary SBLI. This is likely due to the considerably larger viscous dissipation in the corner boundary layer and/or because the turbulent streaks that result in pressure fluctuations are located farther away from the floor. Moving downstream, the evolution of the corner RMS pressure profile is largely similar to that of the primary SBLI. There is a rise to a distinct peak unsteady value of $\sigma_p/\bar{p}_w = 0.032$ at the corner intermittent region, which occurs at the same streamwise position as in the primary SBLI ($x/\delta = -0.8$). Interestingly, this location is virtually coincident with the upstream periphery of the corner vortex structure shown in Figure 23(b). This may serve as the first indication that the corner vortex drives the unsteady shock motion in corner SBLI for low back pressures. There is a

drop in $\sigma_p/\bar{p}_w$ in the region within the core of the corner vortex, followed by a downstream rise. Interestingly, this downstream increase occurs near the downstream periphery of the corner vortex. As previously noted, there are similar instances of a second peak in $\sigma_p/\bar{p}_w$ documented in the fin SBLI studies of Alvi & Settles [27] beneath the separation vortex seen there. Hence, it is hypothesized that the downstream peak in normalized RMS pressure is also caused by the separation vortex. However, there is still a possibility that this second peak in $\sigma_p/\bar{p}_w$ occurs because of the transducer's proximity to the reattachment location. While this ambiguity will be resolved in the following discussion of trends with increased back pressure, the work of Bisek [34] also showed the existence of a peak in $\sigma_p/\bar{p}_w$ just downstream of the corner vortex, which strongly corroborates this hypothesis.

Summarily, the preceding discussions show that the streakline features and mean and unsteady wall pressure profiles of the primary SBLI for the mildest back pressure ratio are entirely consistent with behavior of canonical 2D SBLI discussed at length in literature. In contrast, the features of corner SBLI show that it is 3D in the mean. Further, there are strong indications that the unsteady pressure loading there is indeed driven by the corner separation vortex, upon which the separation shock "rides." The following sections investigate if the spectral features of the separation shock motion are consistent with this hypothesis for the 12° ramp configuration.

b. Intermittent region wall pressure time-series

While the RMS pressure profiles in Figure 25(b) help in identifying the streamwise trends and local maximums of unsteady loading in the primary and corner SBLI for reduced back pressures, they say little about the temporal evolution of the unsteady motions themselves. In order to gain a better qualitative understanding of the differences in the characteristic separated flow motions of primary and corner SBLI, the wall static pressure time-series under the intermittent regions of primary and corner SBLI at $x/\delta = -0.81$ are compared over a 5 ms snippet in Figure 26. It can be observed that the wall pressure signatures of both primary and corner SBLI exhibit broadband aperiodic excursions. The excursions in primary SBLI may be divided into two categories with distinct causes. The small amplitude oscillations present throughout the signature are due to the passage of turbulent structures in the boundary layer, while the large amplitude pressure fluctuations evident at $t \approx 2.8\,ms$ and $t \approx 4.5\,ms$ are indicative of the passage of the separation shock foot. As previously discussed, the latter coincides with the dynamic motions of the downstream separation bubble [15]. It should be

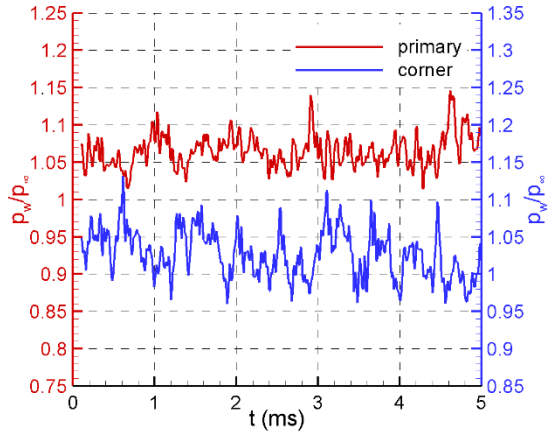

Figure 26. Intermittent region wall pressure time-series comparison for 12° compression ramp case.

noted that the amplitudes of the two fluctuations are not as distinct as in canonical 2D SBLI [15]. This effect is likely due to the increased thickness of the incoming boundary layer at the centerline, which would displace the sonic line upwards by some amount, decreasing the penetration depth of the separation shock foot. Recent direct numerical simulations (DNS) by Priebe et al. [46] have shown that the low-frequency portions of the power spectra can still be well resolved without distinct intermittency, albeit for different reasons than a lifted separation shock foot. There is very little evident periodicity in the passage of the separation shock in the primary SBLI. The corner intermittent region also exhibits similar smaller and larger scale pressure excursions corresponding to boundary layer structure passage and corner shock motions. Interestingly, the large scale excursions in the corner SBLI occur more frequently compared to the primary SBLI, which suggests that the dominant pulsation frequencies are noticeably different between the two SBLI units. The increase in regularity of the shock motion in the corner SBLI supports the earlier supposition that the corner vortex drives the unsteady characteristic motions of the corner SBLI for mild compression strengths.

c. Wall pressure power spectra

Power spectral densities of the wall pressure fluctuations in the primary and corner SBLI intermittent regions were computed to gain additional insights into the characteristic unsteady motions of the separated flows for the mild compression case. The frequency pre-multiplied power spectra for primary (red) and corner (blue) SBLI, both taken from the peak in RMS pressure at $x/\delta = -0.81$, are shown in Figure 27. The magnitudes of the power spectra ($G(f) \times f$) are not normalized, which enables direct comparison of the magnitude of

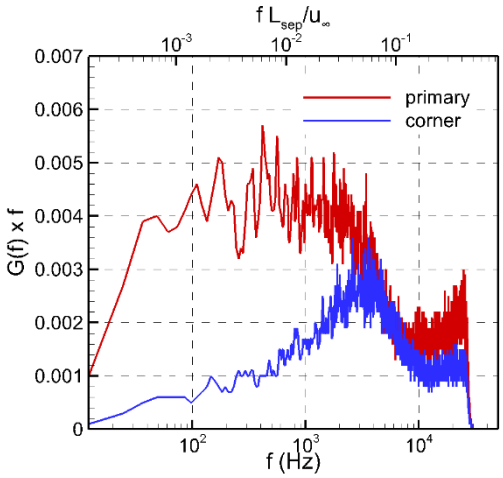

Figure 27. Frequency multiplied power spectra comparison for intermittent regions of 12° compression ramp configuration.

unsteadiness at a given frequency between corner and primary SBLI. It can be discerned from Figure 27 that the energy content of the primary SBLI is distributed over a range of frequencies between $f \approx 100\,Hz$ to $3\,kHz$, a band which corresponds to the low-frequency unsteady motions of the separated flow that have been extensively documented [19]. At the high end of the frequency range, the spectral energy content exhibits a steep dropoff followed by a slight upturn. Note that due to the nature of the data acquisition system, the pressure signal is low-passed at 25 kHz before it is acquired, and it is subsequently concluded that this upturn is in fact due to jitter in the shock motion due to the passage of turbulent structures and not an effect of aliasing. The strong attenuation evident at $f = 25\,kHz$ is an artifact of this low-pass filtering. The broadband nature of the spectral energy content in the primary separation is expected from the seemingly irregular pressure fluctuations seen in the wall pressure time series of Figure 27. The corresponding Strouhal number ($St_L = \frac{f L_{sep}}{u_\infty}$) based on the separation distance length scale $L_{sep} = 8.1\,mm$ (here defined as the streamwise distance between the measured intermittent location and the compression ramp edge) is also shown in Figure 27. It

can be observed that the primary SBLI unsteadiness extends over $St_L \approx 0.001 - 0.05$ with a peak at $St_L \approx 0.01$. This range and peak St_L show good agreement with previous compilations of canonical 2D SBLI. However, it should be noted that the magnitude of the power spectrum between these two normalized frequency bounds is considerably lower than those observed in literature [15]; this may arise due to the centerline boundary layer distortion or the presence of the corner SBLI.

When examining the corner intermittent region power spectrum in Figure 27, it is evident that the energy distribution is considerably more focused than that of the primary separation, exhibiting a distinct spectral peak at $f \approx 3.6\,kHz$. The relatively narrow bandwidth of dominant frequencies in the corner supports the increased periodicity of the transient mechanical loading suggested by the wall pressure time trace of Figure 26. The corresponding St_L is computed with the same L_{sep} length scale used in the primary separation and shows that the corner SBLI pulsations range between $St_L \approx 0.02 - 0.1$, with a peak Strouhal number of $St_L \approx 0.050$. While these values are in line with expectation for SBLI, it should be noted that there is still a good deal of uncertainty regarding the appropriate length scale for computing St_L for a highly 3D interaction such as the corner SBLI. In light of the present hypothesis that corner vortex pulsations drive the unsteady separation shock motions, there is a particular interest in determining if the streamwise vortex length can also provide a consistent Strouhal number. Considering the peak $\sigma_p/\bar{p}_w$ are observed at the upstream and downstream peripheries of the corner separation vortex, the distance between the two transducers measuring the peaks in $\sigma_p/\bar{p}_w$ was used as an appropriate length scale to delineate the vortex size ($L_v = 7.3\,mm$). With this length scale, the corresponding peak Strouhal

number was determined to be $St_L \approx 0.035$. It should be noted that similar peak Strouhal number values have been documented in sharp fin SBLI studies, where the separation vortex dimensions were used as the appropriate length scale. Thus, the power spectra of the corner SBLI is still consistent with the hypothesis that the corner vortex pulsations drive the separation shock motions.

When comparing the relative magnitudes of the primary and corner SBLI power spectra, it can be observed that the corner SBLI magnitude is consistently smaller than that of the primary SBLI. This may be due to the swept nature of the separation shock in the corner, and/or the relatively reduced $\sigma_p/\bar{p}_w$ magnitude in the incoming corner boundary layer discussed previously. Interestingly, in Figure 27 the two spectra exhibit very similar decay between $f \approx 3.6 - 10\ kHz$. While this observation may be purely coincidental, the possibility of this overlap being a result of some dispersive coupling between the corner and primary SBLI units (wherein the disturbances in this frequency range are mutually amplified by the two separation units) cannot be ruled out here. If the dispersive coupling actually exists and happens to persist at all back pressures, then it has significant consequences in unstart physics, where these dispersive interactions between the different separated flow units may prove to be a vital channel for inducing nonlinear growth of separated flow.

It is also interesting to examine how the observed power spectrum of wall-pressure fluctuations at the corner SBLI intermittent region compares with that of the recent LES efforts of Bisek [34] performed at a significantly lower Re_θ $(3000 - 5300)$. This comparison will help to further examine the use of different length scales in computing the Strouhal number in corner SBLI as well as illuminate the similarities and differences that arise from differences in

Re_θ. The frequency pre-multiplied corner SBLI intermittent region power spectrum shown in Figure 27 is compared directly with the work of Bisek [34] for two separation length scales (L_{sep} and L_v), as depicted in Figure 28. The relative smoothness of the LES spectra is because the simulations were performed over many flow time scales. Note that the magnitude of each power spectral density ($G(St_L) \times St_L$) is normalized by area (σ_p) beneath each spectrum over the overlapping Strouhal number range of the two studies for ease of comparison. Whereas the separation length scale L_{sep} was used for the calculation of the Strouhal number in Figure 28(a), the streamwise length between the peaks in $\sigma_p/\bar{p}_w$ on the peripheries of the corner vortex (L_v) was used in Figure 28(b). It can be observed that the experimental power spectra and those of LES agree with one another for both length scales. They show similar qualitative trends, and span almost the same Strouhal number range for dominant pulsations. The values

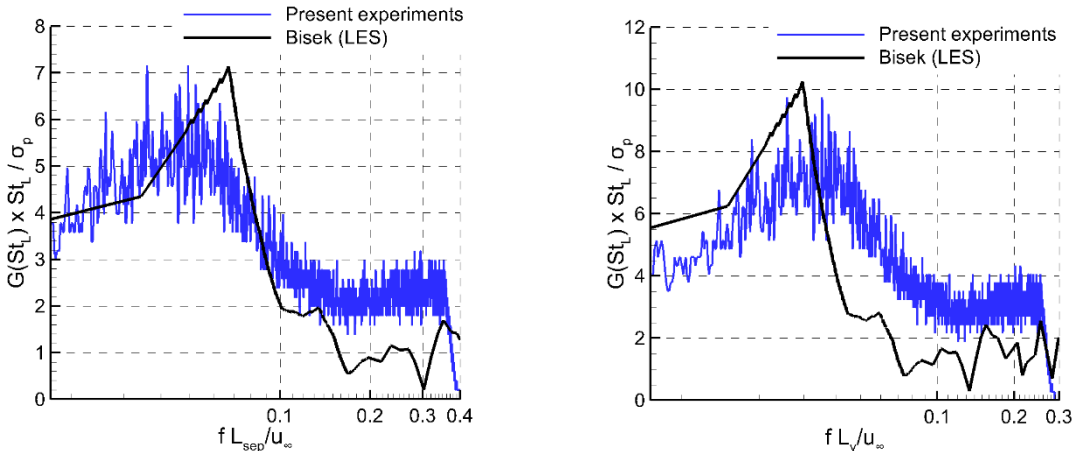

(a) (b)

Figure 28. Comparison of nondimensional corner unsteadiness frequencies (a) using separation length scale (b) using vortex length scale.

of the peak Strouhal numbers calculated using L_{sep} are 0.050 and 0.067 for the present work and LES, respectively. The corresponding peak Strouhal numbers determined using L_v are 0.035 and 0.030 for the present work and LES, respectively. This similarity in the power spectra and the peak non-dimensional frequencies is noteworthy since the difference in Re_θ between the two studies is nearly an order of magnitude. The closer agreement between peak Strouhal numbers using L_v seems to indicate that the use of vortex length scale is more appropriate than L_{sep} for corner SBLI for these two studies, although it should be noted that a similarity in peak Strouhal numbers across only two studies does not constitute the determination of an appropriate characteristic length for normalizing the unsteady frequencies of corner SBLI. A more careful examination of the evolution of the corner power spectra across a range of inflow conditions and back pressure ratios will likely prove useful in determining the role of the corner vortex in driving the unsteadiness of the corner SBLI.

4. Cross-coherence and driving mechanisms of shock unsteadiness

As the aforementioned results suggest that the corner vortex drives the separated shock motions at mild back pressure ratios, it will prove prudent to investigate what drives the corner vortex motions themselves. Like in previous works conducted on 2D SBLI, investigations were made to study the response of the separation shock motion to the pressure fluctuations originating from the incoming boundary layer as well as from the downstream corner vortex. To elucidate how the pressure fluctuations at different frequencies spectrally couple with separation shock motion, two-point cross-coherence studies were performed individually between the intermittent region and the upstream transducer signals, and intermittent region

and downstream transducer signals, where the transducers were separated by $x/\delta \approx 0.4$ from the intermittent region. To compare how the primary and corner SBLI units respond to upstream and downstream perturbations, the primary and corner SBLI cross-coherence spectrum are shown in Figure 29.

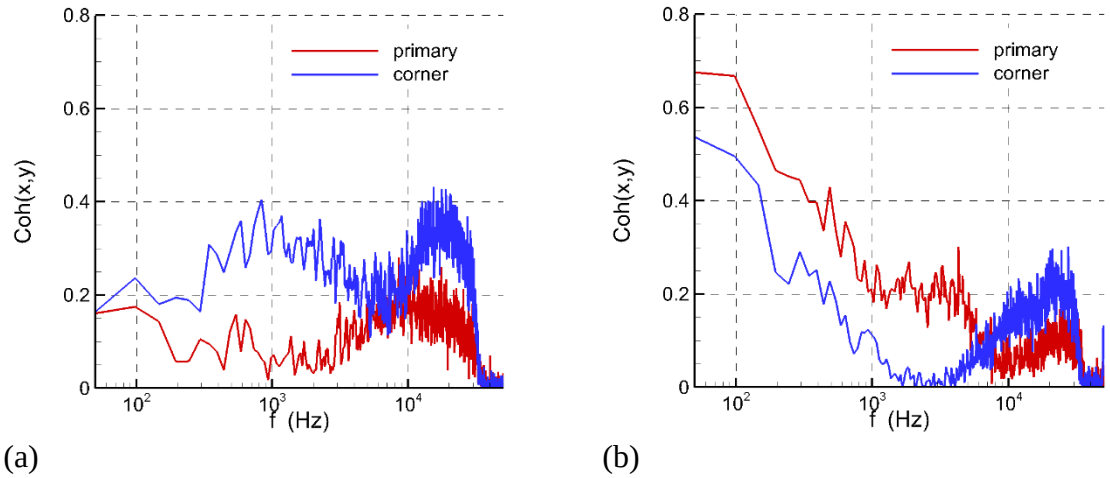

Figure 29. Cross-coherences of wall pressure fluctuations of primary and corner SBLI intermittent regions with various flowfield locations (a) incoming boundary layer (b) downstream separated flow.

Figure 29(a) shows the spectrum of cross-coherence between the intermittent region ($x/\delta = -0.81$) and the incoming boundary layer ($x/\delta = -1.26$) for the primary and corner SBLI units. The frequency range of interest in this study corresponds to the pulsation frequencies of the respective separated flows shown in Figure 27. It can be observed that the cross-coherence magnitude of the primary SBLI remains below ≈ 0.1 over the entire unsteadiness frequency range ($100\,Hz - 3\,kHz$). This shows that the separation shock motion is fairly decoupled from turbulent fluctuations in the incoming boundary layer. In

contrast, the corner separation shock exhibits much larger cross-coherence with the incoming boundary layer fluctuations. The cross-coherence value ranges between $\approx\ 0.25 - 0.4$ over the unsteadiness frequency range of the corner, which suggests a significantly stronger coupling between the incoming boundary layer fluctuations and the unsteady shock motions there. This difference between the degree of coupling evident between the primary and corner SBLI with their respective incoming boundary layers may arise due to the stark difference in the structures of the incoming boundary layers themselves. The apparent coherence of the streamwise vortices in the incoming corner boundary layer discussed by Davis et al. [30] is unlike anything seen in a canonical turbulent boundary layer, and would act to explain the increased degree of coupling between fluctuation in the incoming corner boundary layer and the corner SBLI. It should be noted, however, that the increased three-dimensionality of the corner SBLI necessitates that the results of a two-point cross-coherence limited to the near wall region be interpreted with caution.

Figure 29(b) depicts the corresponding cross-coherence between the downstream separated flow ($x/\delta = -0.36$) and the intermittent region ($x/\delta = -0.81$). It can be observed that the magnitude of cross-coherence in the primary SBLI is consistently larger than 0.2 throughout the unsteadiness frequency band. This value is consistent with the DNS work by Priebe & Martín [46], who conducted cross-coherence studies of a similar nature in a Mach 2.9 flow over a $24°$ compression ramp at $Re_\theta = 3000$. The corresponding value of cross-coherence in corner SBLI is always between $0 - 0.1$. It should be noted that the separated flow topology of corner SBLI is highly three-dimensional, as noted previously. Thus, having a considerably smaller cross-coherence at a specific location in corner separated flow may not

prove that the separated flow pulsations within the corner do not couple appreciably with separation shock motion.

5. Intermediate conclusions for mild back pressure ratios

Previous studies into unstart dynamics have clearly shown that the unstart shock system responds as a single coherent system to the upstream and downstream perturbations during and after unstart initiation. An important question remains unanswered pertaining to the separation units that precede unstart initiation, namely if they too behave as a single coherent system. The discussion to this point provides valuable insights that can be used to answer this question at mild back pressure ratios. A thorough investigation of the corner separation unit has revealed significantly different mean flow structures (e.g., mean 3D SBLI), mean pressure evolution profiles, and spectral features when compared directly to the companion primary separation unit. Further, the corner separation shock couples very differently to pressure fluctuations in the incoming boundary layer when compared to the primary separation shock, which suggests that these two units could potentially be driven by different mechanisms. The combination of the aforementioned results suggests that the corner and primary SBLI behave as distinct units; in other words, the shock interactions that eventually lead to the behavior exhibited during unstart begin at a very local level. How these different separation units couple with one another to eventual respond as a single, coherent unit with increasing back pressure ratio will be investigated subsequently.

The preceding discussion also helps to determine if the initial 2D primary separation would remain so with mild back pressure increase. It can be seen that the primary separation

line is straight over more than 80% of the span here; further, the trends in the mean and RMS wall pressure throughout the primary SBLI and the spectral profile of the intermittent region are highly consistent with those of canonical 2D SBLI that are documented in literature. From these observations, it seems accurate to conclude that the primary separation still remains largely a 2D SBLI at mild back pressures. It remains to be seen how the 2D nature of the primary SBLI will evolve with an increasing adverse pressure gradient in the presence of the companion corner SBLI.

B. Increasing back pressure ratios

1. Surface streakline visualization evolution with increasing back pressure ratios

a. Time-averaged streakline visualization evolution

The results of the time-averaged streakline visualization method are shown for the ramp angles of 16°, 20°, and 24° in Figure 30, which corresponds to the strengthening of the unstart shock system with combustion-induced heat release. For ease of comparison, the results of the mild back pressure ratio case are included again as Figure 30(a).

As the back pressure is increased from the mild case in Figure 30(b) - Figure 30(d), the corner and primary SBLI units exhibit several interesting changes from (and commonalities with) the 12° ramp case. In the primary SBLI, there is a notable increase in the three-dimensionality of the primary separation line as ramp angle increases, and the primary separation exhibits footprints of tornado-vortices present for all ramp angles above 12°. Interestingly, the primary separation line is pulled out toward the centerline in a curved pattern that stretches in the upstream direction with increasing back pressure. The extents of the

primary and corner separations both increase significantly with ramp angle, owing to the increasing magnitude of the shock-induced adverse pressure gradient. While the corner separation line is displaced upstream with increasing ramp angle, the extent of corner vortex

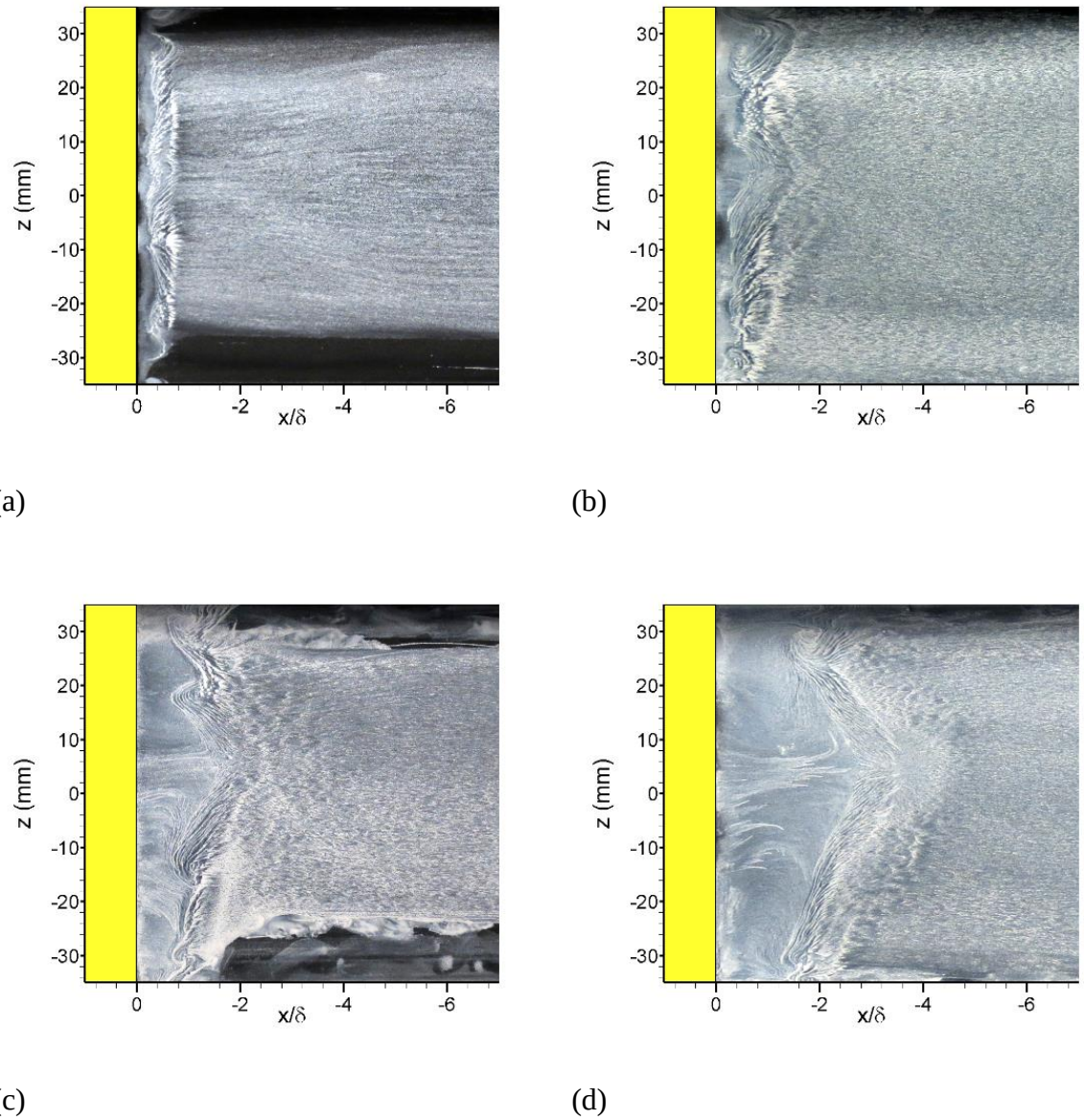

Figure 30. Full-span top views of time-averaged streakline visualizations for various compression ramp configurations, from Funderburk and Narayanaswamy [39] (a) 12° (b) 16° (c) 20° (d) 24°.

appears to remain relatively constant over the range of back pressures employed. This observation is also corroborated with the vortex length determined using RMS wall pressure profiles to be discussed subsequently, and suggests that the primary separation does not appear to influence the size of the corner vortices to a significant extent.

b. Unsteady streakline visualization evolution

Snapshots of the unsteady streakline visualizations for increasing back pressure ratio are shown in Figure 31. For all back pressure ratios, the observed flow features and their extents agree very well with those of the time-averaged streakline visualizations. Therefore, despite the sidewall mounted nature of the unsteady streakline visualization, it is expected that the method provides an accurate depiction of the SBLI flowfield kinematics. The unsteady streakline visualization method also enables observation of the reattachment location on the ramp face ($2 > x/\delta > 0$), which was not possible using the time-averaged method.

For all compression ramp angles above $12°$, the increased three-dimensionality of the primary separation becomes even more apparent in Figure 31. As the ramp angle is increased to $16°$, secondary vortices form at either edge of the primary separation near where it meets the junction boundary layer. These secondary vortices occur just inboard of their respective corner separation vortices, and entrain nearby fluid from the primary separation (example streaklines and their directions are shown in Figure 31(b) to display this effect). In return, the secondary vortex feeds fluid into the corner separation vortex. As the back pressure is increased further in Figure 31(c), the corner separation vortex begins to directly entrain fluid from the

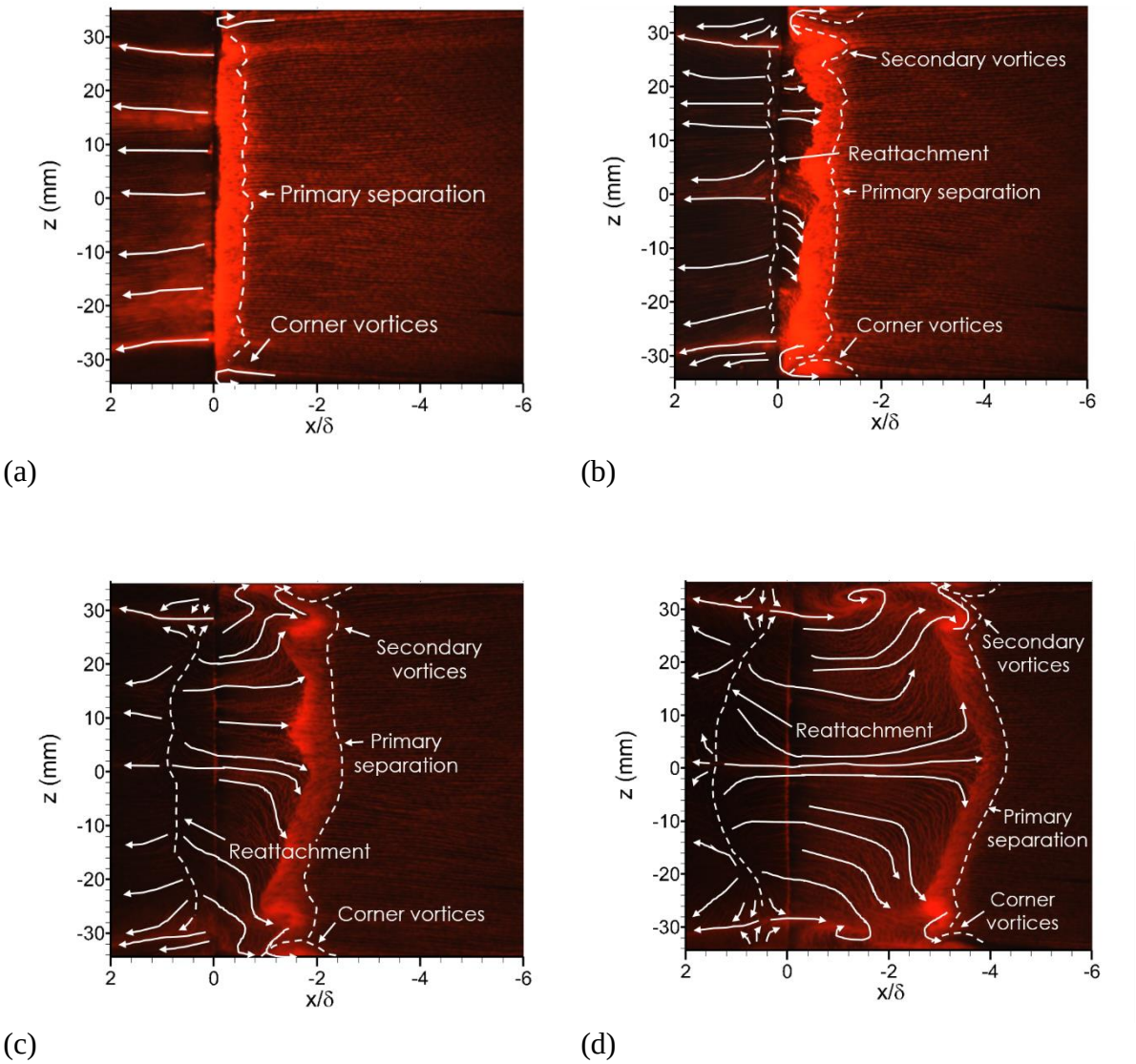

Figure 31. Annotated full-span top views of unsteady streakline visualizations for various compression ramp configurations, (a)12° (b) 16° (c) 20° (d) 24°.

edge of the primary separation. Pockets of recirculation also begin to form downstream of the secondary vortices in Figure 31(d).

The reattachment lines and post-reattachment streaklines visible in Figure 31 seem to echo the behavior of the upstream flow at a given spanwise location for each compression

strength. The reattachment line of the 12° and 16° cases in Figure 31(a) and Figure 31(b) are nominally two dimensional along the bulk of the span (the reattachment line of the 12° case in Figure 31(a) occurs very near to the ramp corner, and is subsequently not highlighted). Dividing streaklines near the top and bottom corner junctions ($z \approx \pm 30\ mm$) separate the core reattachment/ramp face flows from a corner flow that is highly 3D by comparison. As the back pressure ratio is increased further in Figure 31(c) and Figure 31(d), the reattachment line begins to curve downstream near the centerline and stand off from the compression ramp corner, mirroring the primary separation line for these ramp angles. Transverse flow toward the corner junction dividing streaklines is also evident from either side, and increased three-dimensionality in the post-reattachment streaklines along the ramp face is present for the higher ramp angles.

While the results displayed in Figure 31 are certainly revealing in terms of the kinematics near the floor, they must be interpreted with caution due to the heavy three-dimensionality of the SBLI flowfield at higher back pressures. For the purposes of this work it is best to treat these results as a purely qualitative addition to the time-averaged streakline visualizations. However, a couple of interesting conclusions can be drawn from these results which were not immediately visible using the time-averaged method. First, in at least the near-floor regions, the corner vortex plays a more significant role for increased back pressure ratios; almost every streakline visible in the SBLI is eventually entrained by the corner vortex for a ramp angle of 24°, as shown by the zoomed-in top view of the corner flow presented in Figure 32. Second, although the corner vortex continually entrains pigment from the global SBLI, it does not become brighter over the duration of a run. This suggests that the accumulated

pigment mixture is ejected out and over the global SBLI. This finding would be consistent with the aforementioned notion that the corner vortex is the separation vortex of the glancing sidewall SBLI, although this requires further investigation along the sidewall or using a planar method to be sure.

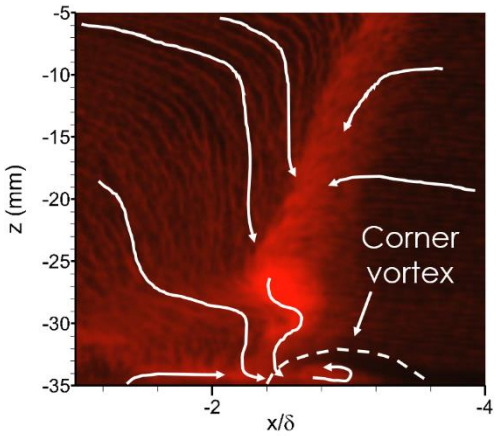

Figure 32. Annotated corner top view of unsteady streakline visualization for 24° compression ramp configuration.

2. Wall pressure measurement evolution with increasing back pressure ratios

a. Mean wall pressure evolution

Figure 33 displays the evolution of the mean wall pressures at each transducer position normalized by the static pressure in the incoming turbulent boundary layer across the range of compression strengths, averaged over three independent experimental runs each.

As the back pressure is increased, the earlier streakline visualizations revealed that the separation shock is pulled out at the centerline and the corner separation lags behind slightly at a distance downstream. This is also observed in the mean pressure profiles of Figure 33(b) – Figure 33(d), which show that the pressure first begins to increase at a progressively upstream location in the primary SBLI when compared to corner SBLI. Further, as the extent of the

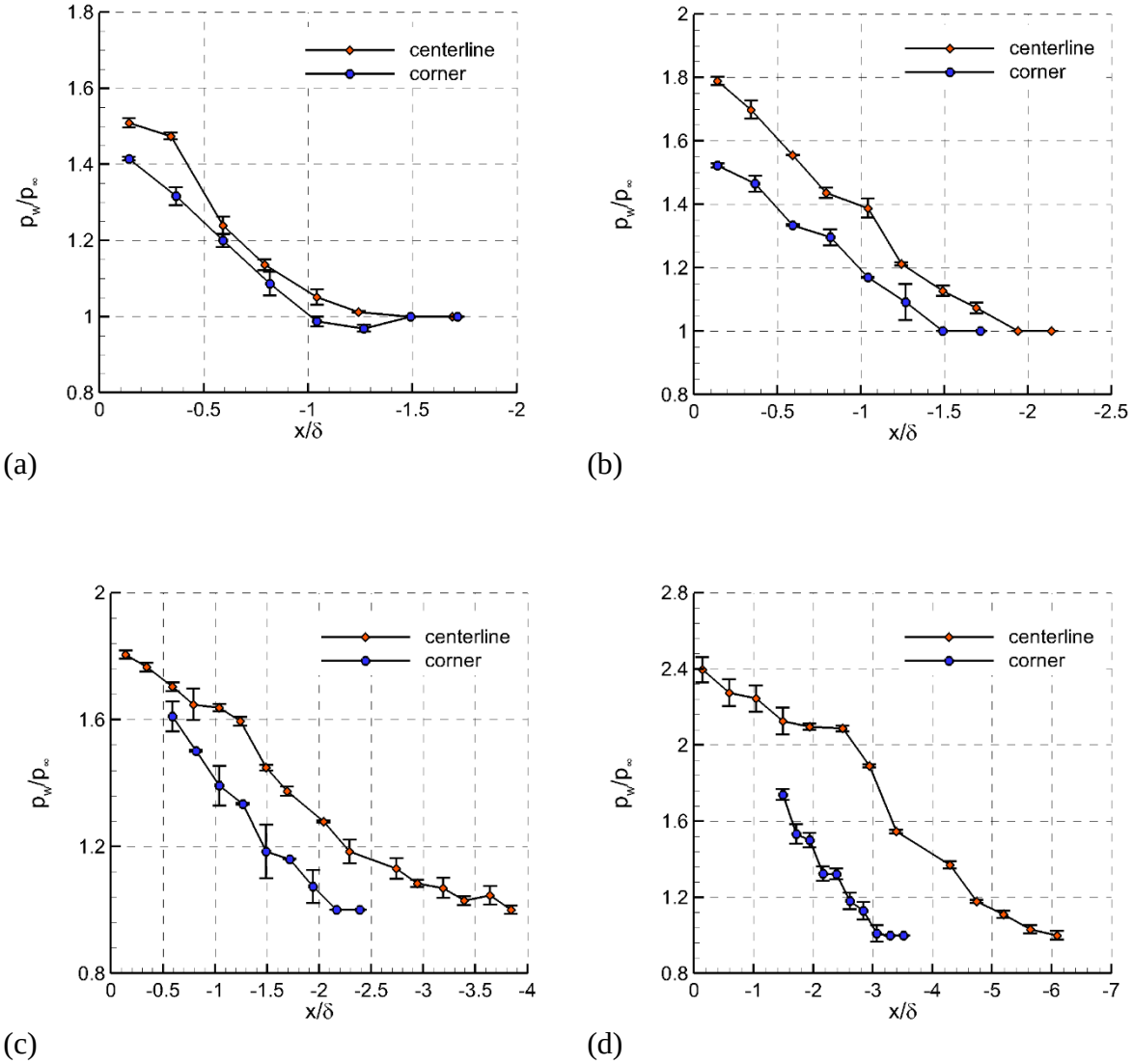

Figure 33. Mean wall pressures profiles for various compression ramp configurations (a) 12° (b) 16° (c) 20° (d) 24°.

primary separated flow increases with back pressure, the pressure gradient along the primary separation is considerably reduced. For example, whereas the wall pressure increases by 60% over 1δ for the 12° case, the pressure increases by 100% over 3δ for the 24° case. Interestingly, two distinct regions of pressure gradients in Figure 33(d) can be observed – a

larger pressure gradient region between $-2 \geq x/\delta \geq -4$ that corresponds to the intermittent region of the SBLI, and a smaller pressure gradient region for $x/\delta \geq -2$, which corresponds to the separated flow region. Further, Figure 33(a) – Figure 33(d) show that the intermittent region exhibits similar pressure gradient values for all back pressures considered. Similar observations on the dichotomy of pressure gradient along the SBLI and the similarity of the gradients in the intermittent region over different shock strengths were also made by Dolling & Or [26] in 2D SBLI.

b. RMS pressure evolution

The streamwise evolutions of the wall pressure fluctuations in the primary and corner SBLI with increasing adverse pressure gradient are shown in Figure 34. Note that the RMS pressure at each transducer is again normalized by its respective mean shown in Figure 33, to enable direct comparison between various streamwise positions and compression strengths. Again note that the results of the mild back pressure case are included as Figure 34(a) for comparison's sake.

Considering the profiles of $\sigma_p/\bar{p}_w$ as the back pressure is increased in Figure 34(b) – Figure 34(d), it can be observed that the trends exhibited are similar to those of the 12° case. Both the primary and corner intermittent regions (identified by the most upstream peak in $\sigma_p/\bar{p}_w$) move upstream with ramp angle, as expected and suggested by the streakline visualizations. Further, the locations of the intermittent regions consistently occur just upstream of the initial separation point in the primary SBLI, and on the upstream periphery of the corner vortex for the corner SBLI (as suggested by the unsteady streakline visualizations

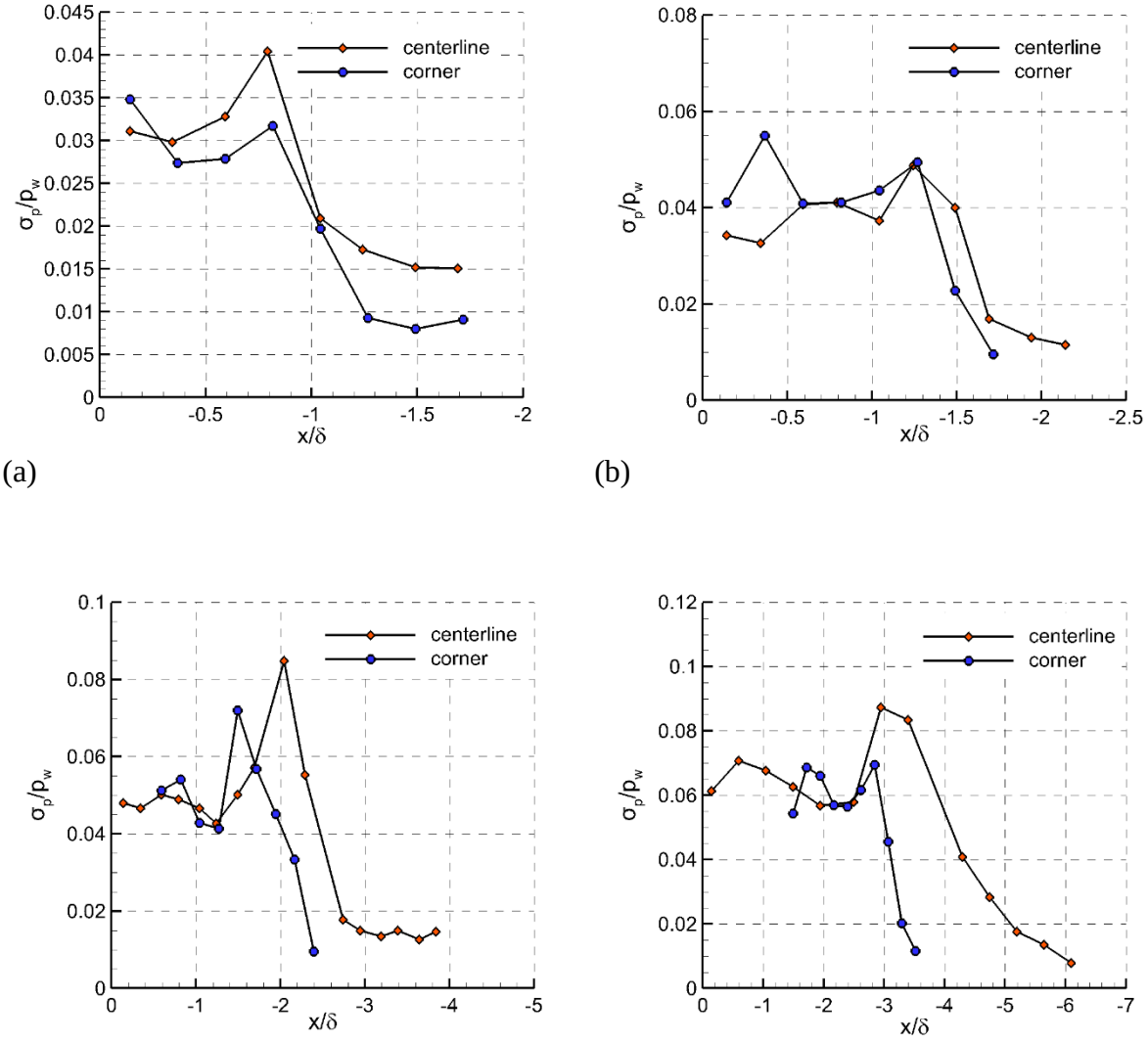

Figure 34. RMS pressure profiles for various compression ramp configurations (a) 12° (b) 16° (c) 20° (d) 24°.

of Figure 31). Top views of the intermittent region transducers (and those used for subsequent cross-coherence calculations) are superimposed on the unsteady streakline visualizations in Figure 38 (Appendix).

The RMS pressure curves depicted in Figure 34 also enable the determination of length scales that will later prove to be necessary in the calculation and comparison of normalized frequency spectra. Here, the separation length L_{sep} is defined as the streamwise distance from the compression ramp leading edge to the intermittent region. As previously noted, the two distinct peaks in pressure fluctuation present in the corner lend themselves to the definition of a separate vortex length scale L_v, which is the streamwise distance between the upstream and downstream peaks that are observed to coincide with the corner vortex edges. Table 4 shows the values of L_{sep} and L_v for each configuration that were calculated from Figure 34; note that L_{sep} corresponds to the *primary* separation distance measured using centerline $\sigma_p/\bar{p}_w$ data to identify the intermittent region.

Table 4. Separation and vortex length scales for various compression ramp configurations.

Ramp angle	$L_{sep}(mm)$	$L_v\ (mm)$
12°	8.1	8.1
16°	12.4	8.9
20°	20.4	6.7
24°	29.4	11.2

From Table 4, the increase in primary separation extent with ramp angle is readily evident. Interestingly, no such pattern is evident in the corner vortex length, with the size remaining relatively constant. This supports the earlier trend observed in the streakline visualization, and suggests that while the primary separation extent is modified by increasing shock strength, the corner vortex diameter may respond to different influencing mechanisms such as the corner boundary layer thickness.

c. Wall pressure power spectra evolution

Power spectral densities of the corner and primary SBLI intermittent regions with increasing back pressure ratio were computed in order to gain insights into the development of the characteristic separated flow motions that create the unsteady mechanical loading during unstart. Figure shows the frequency-multiplied power spectrum of the primary and corner SBLI intermittent regions for each ramp angle. The separation length scales from Table 4 were used in the determination of the Strouhal number ($St_{L_{sep}}$), which is also displayed.

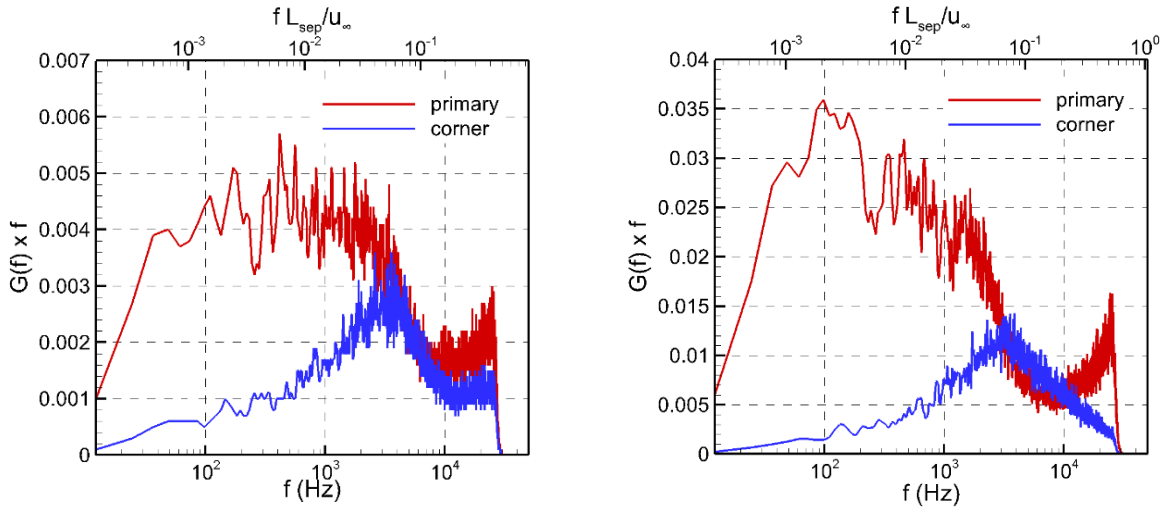

Figure 35. Comparison of pressure power spectra of intermittent regions for various compression ramp configurations (a) 12° (b) 16° (c) 20° (d) 24°.

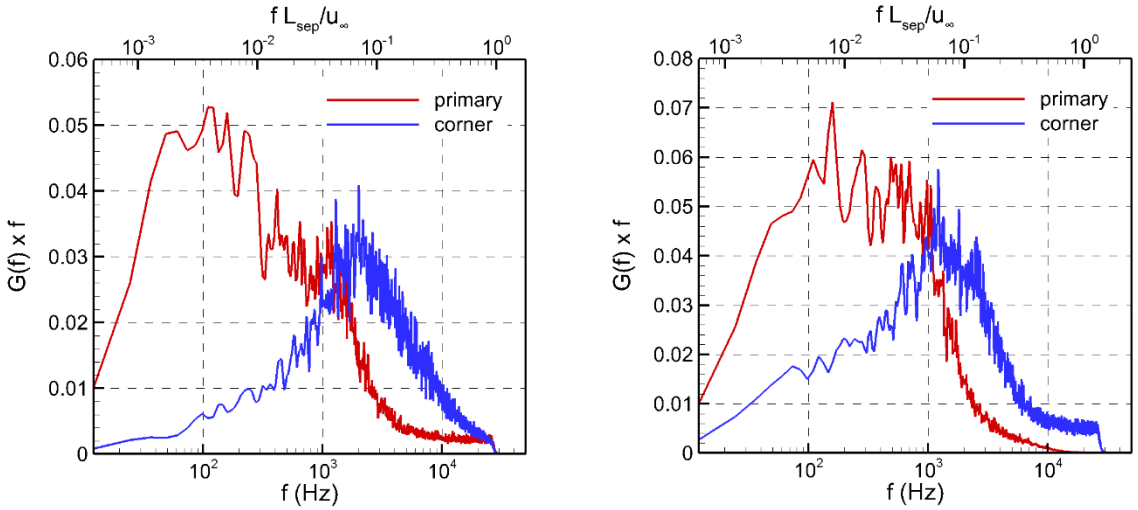

Figure 35 (continued). Comparison of pressure power spectra of intermittent regions for various compression ramp configurations (a) 12° (b) 16° (c) 20° (d) 24°.

As the compression ramp angle is increased, both the primary and corner SBLI exhibit spectral shifts toward lower frequencies. For ease of observation, the peak frequencies and Strouhal numbers of each SBLI are listed in Table 5. Note that the range of peak Strouhal numbers exhibited for the primary SBLI are in line with previous compilations of canonical 2D SBLI. From Table 5, the shift toward low frequency is evident in the corner as the peak frequency consistently decreases with increasing ramp angle. This is not discernable from the centerline data in Table 5 due to the broadband nature of the primary SBLI, and is more easily viewed by comparing Figure(a) with Figure(d), as the dominant frequency range shrinks from $f \approx 100\ Hz$ to $3\ kHz$ at 12° to $f \approx 100\ Hz$ to $1200\ kHz$ at 24°. Interestingly, the dominant corner frequency seems to consistently occur very near where the primary SBLI begins to exhibit spectral decay at higher frequencies, although it remains to be seen whether this result is meaningful or coincidental.

Table 5. Peak frequencies and Strouhal numbers for various compression ramp configurations.

Ramp angle	Primary		Corner		
	$f\ (Hz)$	$St_{L_{sep}}$	$f\ (Hz)$	$St_{L_{sep}}$	St_{L_v}
12°	410	0.0056	3490	0.048	0.048
16°	100	0.0021	3140	0.066	0.047
20°	120	0.0042	1920	0.066	0.022
24°	160	0.0080	1200	0.060	0.023

While the separation scale of the primary SBLI is known, a great deal of uncertainty still remains regarding the choice of an appropriate characteristic length for scaling of the corner SBLI characteristic unsteadiness. Previously, it was shown that both L_{sep} and L_v provided similar values of peak Strouhal number that are consistent with fin SBLI literature. Of the two, L_v was more physically meaningful, as the corner vortex appeared to drive the unsteady separation at low back pressures. Now the question becomes how the peak Strouhal numbers based on L_{sep} and L_v evolve with increasing back pressure; in other words whether or not the corner vortex motions will continue to dominate/drive the characteristic motions of the corner SBLI. To answer this question, the peak Strouhal numbers for different back pressures defined using L_{sep} and L_v are also shown in Table 5. It can be observed that St_{L_v} seems to have closer agreement in values for low back pressures (12° and 16° ramp angles), while higher back pressures exhibit large scatter in St_{L_v} values. Similarly, while the $St_{L_{sep}}$values for 12° and 16° show considerable difference, $St_{L_{sep}}$ appears to collapse evenly at higher shock strengths ($16°, 20°, 24°$). Figure 36 shows this disparity through the nondimensional frequency spectra of the primary and corner intermittent regions at each back pressure for L_{sep} and L_v (note that each spectrum is normalized by the area beneath it for ease

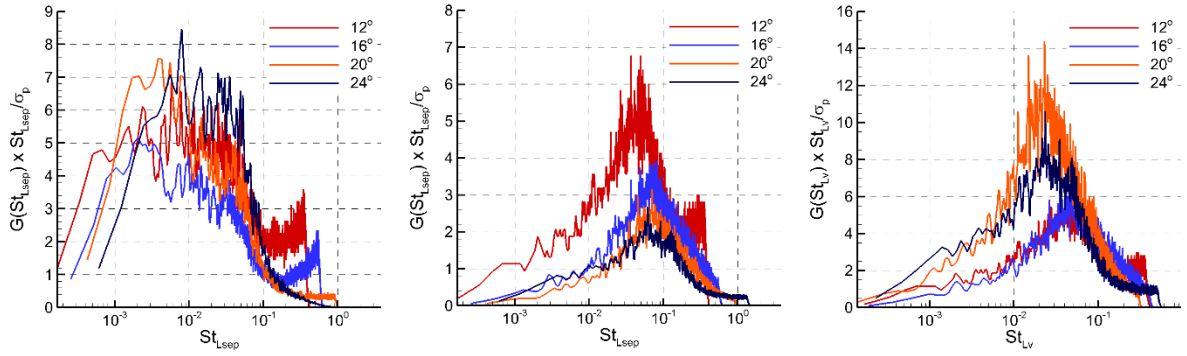

(a) (b) (c)

Figure 36. Power spectra of primary and corner SBLI intermittent regions using L_{sep} and L_v (a) primary SBLI using L_{sep} (b) corner SBLI using L_{sep} (c) corner SBLI using L_v.

of comparison). From Figure 36(a), it is evident that L_{sep} remains the appropriate characteristic length for scaling of the primary SBLI unsteadiness. In contrast, Figure 36(b) and Figure 36(c) show the corner spectra based on the separation and vortex length scales, respectively, and reveal the scatter between higher and lower back pressures discussed previously. The results of Figure 36 and Table 5 suggest that at mild back pressures, L_v appears to scale the characteristic unsteadiness of corner SBLI while L_{sep} scales the corner SBLI unsteadiness neatly at high back pressures. This suggests that the corner SBLI transitions from being a distinct, local unit driven by corner vortex pulsations at low back pressures to an interacting portion of a global separation unit that is influenced by global driving mechanisms; this is highly consistent with the unsteady streakline visualization results of Figure 31, which suggest that fluid from the primary separation bubble is fed into the corner separation vortex for all ramp angles above 12°.

3. Cross-coherence evolution with increasing back pressure ratios

The sources that drive the primary and corner SBLI at different back pressures were studied further to elucidate how the driving mechanisms evolved with an increasing adverse pressure gradient. Two-point cross-coherence studies were performed at each imposed back pressure to determine the response of the separation shock motion to pressure fluctuations originating from the incoming boundary layer and the downstream separated flows. Cross-coherences were performed individually between the intermittent region and upstream transducer pressure signals, and intermittent region and downstream transducer pressure signals, each separated by $x/\delta \approx 0.45$ from the intermittent region.

Figure depicts the cross-coherence spectra of the primary and corner SBLI with the upstream and downstream pressure signals for the range of configurations tested. As the adverse pressure gradient is increased, the trends evident in the cross-coherence spectra of the

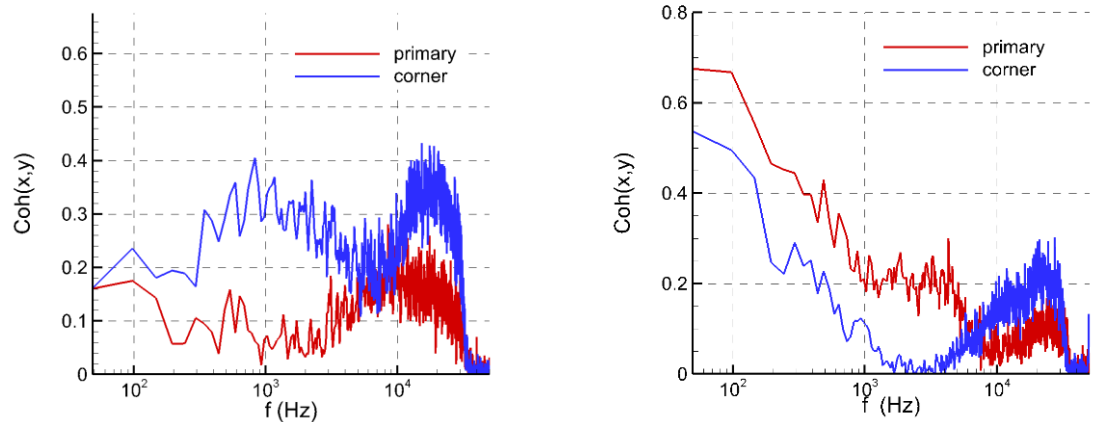

Figure 37. Cross-coherence spectrum of intermittent regions with upstream boundary layer and downstream separation for various compression ramp configurations (a) 12° upstream (b) 12° downstream (c) 16° upstream (d) 16° downstream (e) 20° upstream (f) 20° downstream (g) 24° upstream (h) 24° downstream.

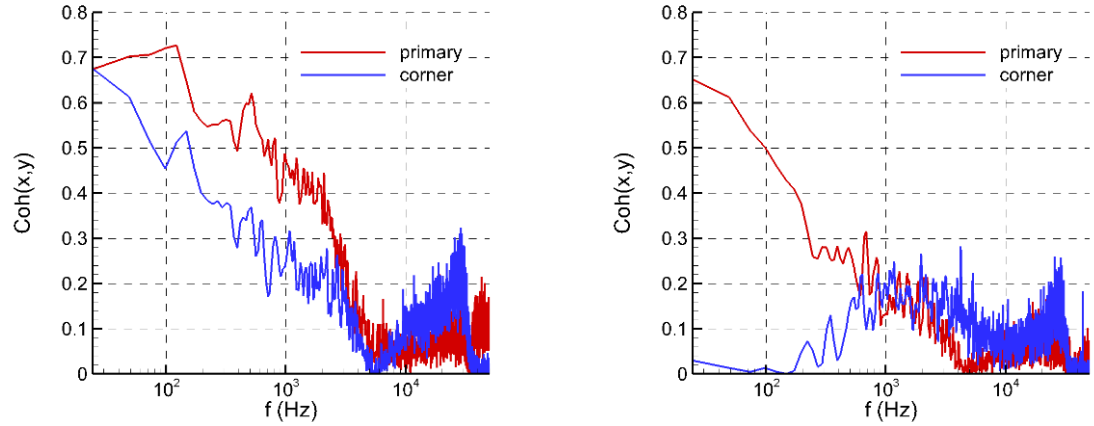

(c)

(d)

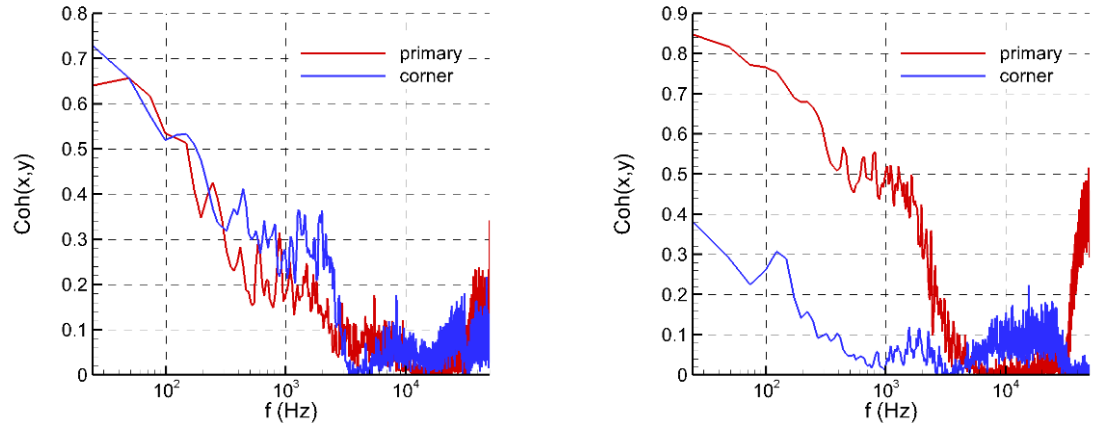

(e)

(f)

Figure 37 (continued). Cross-coherence spectrum of intermittent regions with upstream boundary layer and downstream separation for various compression ramp configurations (a) 12° upstream (b) 12° downstream (c) 16° upstream (d) 16° downstream (e) 20° upstream (f) 20° downstream (g) 24° upstream (h) 24° downstream.

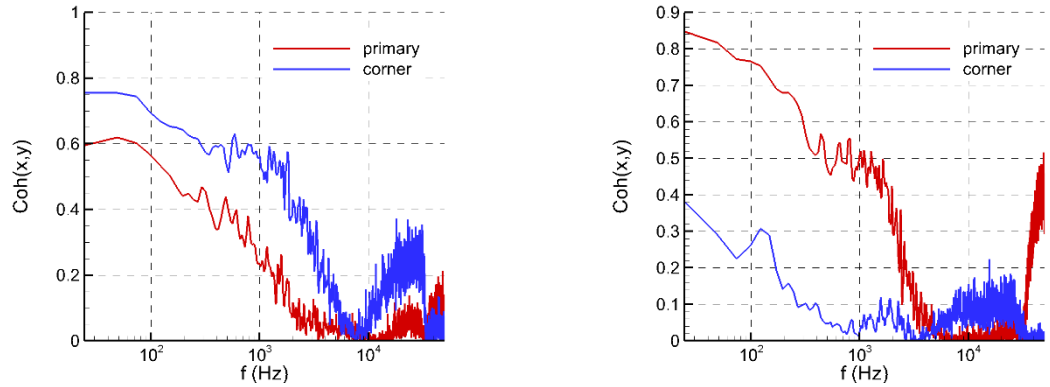

(g) (h)

Figure 37 (continued). Cross-coherence spectrum of intermittent regions with upstream boundary layer and downstream separation for various compression ramp configurations (a) 12° upstream (b) 12° downstream (c) 16° upstream (d) 16° downstream (e) 20° upstream (f) 20° downstream (g) 24° upstream (h) 24° downstream.

primary SBLI remain largely the same in the downstream separation region, as the separation shock motion consistently couples more with the downstream separation. Interestingly, there is also an increasing coupling of the primary separation shock with incoming boundary layer fluctuations with increasing back pressure. Similarly, the corner separation shock begins to couple appreciably with the motions of the downstream corner vortex as well as incoming boundary layer fluctuations as ramp angle increases, such that at 24° it responds nearly equally to the vortex motions and incoming turbulent fluctuations. In Figure(g) and Figure(h), the primary and corner cross-coherence spectra begin to resemble one another, suggesting that the two will respond similarly to perturbation acting almost like a single unit. This observation further strengthens the hypothesis that the corner and primary SBLI have coupled into a coherent unit that responds similarly to the upstream and downstream fluctuations. An important caveat is that both the primary and corner SBLI units are highly 3D even in mean.

Thus, the similarity in coupling of separation shock motion to one downstream location may not be enough to establish that the corner and primary SBLI respond in a like manner to all downstream fluctuations. Similarly, the wall pressure fluctuations in the incoming boundary layer may not capture the global changes in the incoming momentum of non-canonical boundary layers that occur along the corner. Thus, similarity in the shock response to upstream fluctuations should also be treated with caution.

V. CONCLUSIONS AND FUTURE WORK

An experimental investigation has been made into the primary and corner SBLI generated in a rectangular channel flow by compression ramps of various angles at $M_\infty = 2.5$. Selection of the ramp angles follows inviscid pressure ratios representative of a buildup to unstart initiation in a rectangular mixed compression inlet.

Initial boundary layer measurements with the compression ramp removed have revealed a considerable velocity deficit at the centerline, and further investigation using surface streakline visualizations shows a system of reflecting transverse waves which persist into the measurement domain. At present, the effect of these waves cannot be discounted, and it is unknown to what extent the observed results are affected by them. They are an artifact of the distance between the sidewall fences, as they will reflect and process the incoming flow with increased regularity for less wide channels at the same incoming Mach number. However, it is important to keep in mind that the results here are confined to the near-wall region, and that the effects of these waves on the lifted features of the unstart SBLI have not yet been investigated. In the immediate future, experiments of the same nature as the present study with

a wider channel or a single sidewall fence will prove useful in resolving the near-wall effects of the transverse waves on the unstart SBLI, while later planar velocimetry methods will examine any effect on the flow away from the wall. These experiments will also aid in decoupling the effects of area blockage arising due the introduction of the corner flow from the effects of the transverse waves.

With regards to the compression ramp SBLI, time-averaged surface streakline visualization has shown a two-dimensional primary SBLI structure at mild shock strengths, while the presence of a vortex footprint in the corner SBLI indicates a three-dimensional flow structure there. Substantial three-dimensionality develops in the primary SBLI with increasing back pressure ratio, and while both initial separation points move upstream, the size of the corner vortices remains relatively constant.

Additional unsteady surface streakline visualization has revealed that the flow on the downstream ramp face tends to mirror the behavior of the upstream flow, in that the reattachment zone is two-dimensional behind a two-dimensional primary SBLI for reduced back pressure ratios, while the corner ramp flow shows three-dimensionality at all compression strengths. Further, the bulk reattachment line and post-reattachment streaklines show increased three-dimensionality for the higher ramp angles. Interestingly, the corner vortex is seen to play an increased role for higher back pressure ratios, as flow from the primary separation is progressively entrained by it.

Mean wall static pressure measurements show an initial smearing of the adverse pressure gradient in the corner, similar to previous findings. A disparity is evident with respect to pressure gradients in the intermittent regions and downstream separated flows for increased

back pressure ratios. The RMS pressure contours consistently show a single distinct peak along the centerline at the intermittent region, and two peaks in the corner SBLI that are seen to coincide with the upstream and downstream peripheries of the corner vortex. Pressure power spectra reveal that the energy content of the corner unsteady motions is considerably more focused than its counterpart in the primary SBLI, and that the appropriate length scale for the calculation of nondimensional frequency in the corner SBLI may change as the inviscid pressure ratio is increased and the corner SBLI is integrated into the global SBLI. This is consistent with the aforementioned unsteady streakline visualization, which shows that fluid is entrained into the corner vortex from the primary SBLI for higher compression strengths.

Finally, cross-coherences show that the primary shock motion couples more with pressure fluctuations in the downstream separation than the incoming boundary layer for a given ramp angle, although the magnitude of cross-coherence increases between the intermittent region and upstream boundary layer with ramp angle. The corner trends are similar but inverted, as the corner shock motions couple more so with the incoming boundary layer but are increasingly responsive to the motion of the downstream separation with increasing back pressure. The cross-coherence spectra begin to resemble one another as the adverse pressure gradient increases.

The combination of the aforementioned results suggest two distinct stages in the unstart-specific SBLI units, one where the initial primary and corner SBLI act as mutually independent entities at mild shock strengths, and a later stage wherein they are integrated for higher back pressure ratios. This finding could be of great importance during an unstart event, as perturbations in the primary or corner SBLI could be selectively amplified by the entire unit.

Moving forward, the heavy three-dimensionality of the global SBLI present at higher back pressure ratios warrants a closer look with a planar or volumetric velocimetry method. These methods can reveal details about the off-body flow structures and their interactions that wall-limited methods are incapable of resolving, and better characterize the inflow conditions of the present study. Further, while it has been shown that the introduction of the corner SBLI considerably modifies the near-wall primary SBLI for higher back pressure ratios, little is known about the mechanisms through which this modification occurs. Therefore, it will prove prudent to perform similar tests for a canonical 2D SBLI in the same facility to gage any differences from the mean and unsteady characteristics observed here.

REFERENCES

[1] S. Farokhi, Aircraft Propulsion. Second ed., West Sussex: John Wiley & Sons, 2014.

[2] D. Riggins, R. Tackett, T. Taylor and A. Auslender, "Thermodynamic analysis of dual mode scramjet engine operation and performance," *AIAA Paper, 8059,* 2006.

[3] R. H. Graham, Flying the SR-71 Blackbird, Zeneth Press.

[4] B. R. Rich, Skunk Works: A Personal Memoir of My Years at Lockheed, Back Bay Books, 1996.

[5] A. Church, "Air Force World, Second X-51 Test Cut Short," *Air Force magazine,* vol. 94, pp. 17-18, 2011.

[6] A. R. Wieting, "Exploratory Study of Transient Unstart Phenomena in a Three-Dimensional Fixed-Geometry Scramjet Engine," *NASA TN D-8156,* 1976.

[7] J. L. Wagner, K. B. Yuceil, A. Valdavia, N. T. Clemens and D. S. Dolling, "Experimental Investigation of Unstart in an Inlet/Isolator Model in Mach 5 Flow," *AIAA J,* vol. 47, no. 6, pp. 1528 - 1542, 2009.

[8] S. O'Byrne, M. Doolan, S. R. Olsen and A. F. P. Houwing, "Analysis of Transient Thermal Choking Processes in a Model Scramjet Engine," *Journal of Propulsion and Power,* vol. 16, no. 5, pp. 808 - 814, 2000.

[9] S. Laurence, S. Karl, J. Schramm and K. Hannemann, "Transient fluid-combustion phenomena in a model scramjet," *Journal of Fluid Mechanics,* vol. 722, pp. 85 - 120, 2013.

[10] M. A. Frost, D. Y. Gangurde, A. Paull and D. J. Mee, "Boundary-Layer Separation Due to Combustion-Induced Pressure Rise in a Supersonic Flow," *AIAA Journal,* vol. 47, no. 4, pp. 1050-1053, 2009.

[11] R. Korkegi, "Comparison of Shock Induced Two and Three-Dimensional Incipient Turbulent Separation," *AIAA Journal,* vol. 13, no. 4, pp. 534-535, 1975.

[12] K. S. McDaniel and J. R. Edwards, "Simulation of Thermal Choking in a Model Scramjet Combustor," *AIAA 99-3411,* 1999.

[13] K. S. McDaniel and J. R. Edwards, "Three-Dimensional Simulation of Thermal Choking in a Model Scramjet Combustor," *AIAA 2001-0382,* 2001.

[14] G. Masuya, T. Kumoro, A. Murakami, N. Shonozaki, A. Nakamura and O. Murayama, "Ignition and Combustion Performance of Scramjet Combustors with Fuel Injection Struts," *Journal of Propulsion and Power,* vol. 11, no. 2, pp. 301-307, 1995.

[15] D. Dolling, "Fluctuating Loads in Shock Wave/Turbulent Boundary Layer interaction: Tutorial and Update," in *31st Aerospace Sciences Meeting & Exhibit*, 1993.

[16] A. Zheltovodov, "Shock wave/turbulent boundary layer interactions - fundemental studies and applications," *AIAA paper, 96-1977,* 1996.

[17] J. Edwards, "Numerical simulations of shock boundary layer interactions using time-dependent modeling techniques: a survey of recent results," in *46th AIAA Aeropsace Sciences Meeting*, Reno, 2008.

[18] D. V. Gaitonde, "Progress in Shock Wave/Boundary Layer Interactions," in *43rd Fluid Dynamics Conference*, 2013.

[19] N. T. Clemens and V. Narayanaswamy, "Low-Frequency Unsteadiness of Shock/Wave Boundary Layer Interactions," *Annual Review of Fluid Mechanics,* pp. 469-492, 2014.

[20] B. Wang, N. Sandham, Z. Hu and W. Liu, "Numerical study of oblique shock-wave/boundary-layer interaction considering sidwall effects," *Journal of Fluid Mechanics,* vol. 767, pp. 526-561, 2015.

[21] A. Smits and J. Dussauge, Turbulent Shear Layers in Supersonic Flow, Woodbury, NY: AIP, 1996.

[22] R. D. D. Gramann, "Dynamics of Separation and Reattachment in a Mach 5 Compression Ramp Flow," in *AIAA 28th Aerospace Sciences Meeting*, 1990.

[23] M. Kussoy, J. Brown and J. L. W. H. C. Brown, "Fluctuations and Massive Separation in Three-Dimensional Shock Wave/Boundary Layer Interactions," in *2nd International Symposium of Transport Phenomena in Turbulent Flows*, Tokyo, Japan, 1987.

[24] M. Erengil and D. Dolling, "Unsteady Wave Structure near Separation in a Mach 5 Compression Ramp Interaction," *AIAA Journal,* vol. 29, no. 5, pp. 728-735, 1990.

[25] M. Erengil and D. Dolling, "Correlation of Separation Shock Motion with Pressure Fluctuations in the Incoming Boundary Layer," *AIAA Journal,* vol. 29, no. 11, pp. 1868-1877, 1991.

[26] D. Dolling and C. Or, "Unsteadiness of shock wave structure in attached and separated compression ramp flows," *Experiments in Fluids,* vol. 3, pp. 24-32, 1985.

[27] F. Alvi and G. Settles, "Physical Model of the Swept Shock Wave/Boundary-Layer Interaction Flowfield," *AIAA Journal* , vol. 30, no. 9, pp. 2252-2258, 1992.

[28] M. Erengil and D. Dolling, "Effects of Sweepback on Unsteady Separation in Mach 5 Compression Ramp Interactions," *AIAA Journal,* vol. 31, no. 2, pp. 302-311, 1993.

[29] S. Garg and G. Settles, "Wall Pressure Fluctuations Beneath Swept Shock/Boundary Layer Interactions," in *AIAA 30th Aerospace Sciences Meeting,* Reno, NV, 1993.

[30] D. Davis and F. K. G. Gessner, "Experimental and Numerical Investigation of Supersonic Turbulent Flow Through a Square Duct," *AIAA Journal,* vol. 24, no. 9, pp. 1508-1515, 1986.

[31] D. Burton and H. B. P. Babinsky, "Experimental Investigation into Parameters Governing Corner Interactions for Transonic Shock Wave/Boundary Layer Interactions," *AIAA Paper, 871,* 2010.

[32] P. Bruce, D. Burton, N. Titchener and H. Babinsky, "Corner effect and separation in transonic channel flows," *Journal of Fluid Mechanics,* vol. 679, pp. 247-262, 2011.

[33] H. Babinsky, J. Oorebeek and T. Cottingham, "Corner effects in reflecting oblique shock-wave/boundary layer interactions," in *51st AIAA Aerospace Sciences Meeting,* Dallas/Ft. Worth, 2013.

[34] N. Bisek, "Sidewall Interaction of a Supersonic Flow over a Compression Ramp," in *53rd AIAA Aerospace Sciences Conference,* 2015.

[35] A. Hegde, "Experimental Investigation into Shock Induced Corner Boundary Layer Separation (Masters Thesis)," Raleigh, NC, 2014.

[36] J. Bendat and A. Piersol, Random Data, 2nd Edition, John Wiley & Sons, 1986.

[37] S. Sun and M. Childs, "A Modified Wall Wake Velocity Profile for Turbulent Compressible Boundary Layers," *Journal of Aircraft,* vol. 10, no. 6, pp. 381-383, 1973.

[38] M. Funderburk and V. Narayanaswamy, "Experimental investigation of primary and corner shock boundary layer interactions at mild back pressure ratios," *Physics of Fluids Paper 086102,* vol. 28, 2016.

[39] M. Funderburk and V. Narayanaswamy, "Experimental Investigation of Shock Boundary Layer Interactions to Unravel Inlet Unstart Physics," in *AIAA Aviation*, Washington, DC, 2016.

[40] A. Hegde, M. Funderburk, J. Hill and V. Narayanaswamy, "Experimental Investigation into Shock Induced Corner Boundary Layer Separation," in *AIAA Aviation*, Dallas, TX., 2015.

[41] D. Burton and H. Babinsky, "Corner separation effects for normal shock wave/turbulent boundary layer interactions in rectangular channels," *Journal of Fluid Mechanics,* vol. 707, pp. 287-306, 2012.

[42] N. Titchener and H. Babinsky, "Shock Wave/Boundary-Layer Interaction Control Using a Combination of Vortex Generators and Bleed," *AIAA Journal,* vol. 51, no. 5, pp. 1221-1233, 2013.

[43] M. Rybalko, H. Babinsky and E. Loth, "Vortex Generators for a Normal Shock/Boundary-Layer Interaction with a Downstream Diffuser," *Journal of Propulsion and Power,* vol. 28, no. 1, pp. 71-82, 2012.

[44] G. Settles, T. Fitzpatrick and S. Bogdonoff, "Detailed Study of Attached and Separated Compression Corner Flowfields in High Reynolds Number Supersonic Flow," *AIAA journal,* vol. 17, no. 6, pp. 579-585, 1979.

[45] F. Thomas, C. Putnam and H. Chu, "On the mechanism of unsteady shock oscillation in shock/wave turbulent boundary layer interactions," *Experiments in Fluids,* vol. 18, pp. 69-81, 1994.

[46] S. Priebe and M. Martin, "Low-frequency unsteadiness in shock wave-turbulent boundary layer interaction," *Journal of Fluid Mechanics,* vol. 699, pp. 1-49, 2012.

APPENDIX

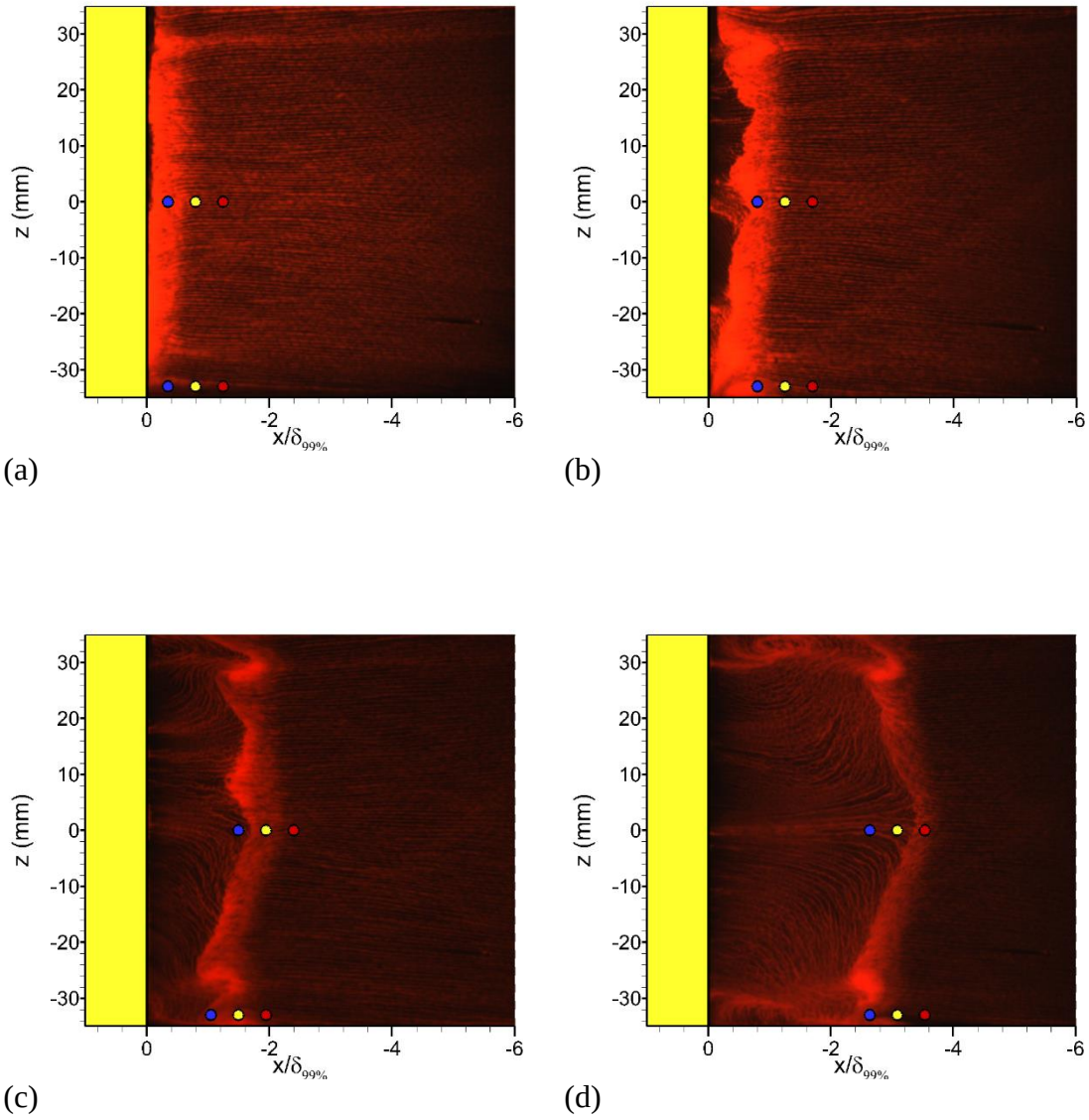

Figure 38. Top views of intermittent region transducers (yellow) superimposed on unsteady streakline visualizations for various compression ramp configurations, upstream (red) and downstream (blue) cross-coherence transducers also shown. (a)12° (b) 16° (c) 20° (d) 24°